

RESEARCH

Open Access



# Islet cell spheroids produced by a thermally sensitive scaffold: a new diabetes treatment

Xueting Yao<sup>1,2,7</sup>, Zehua Gong<sup>3</sup>, Wenyan Yin<sup>4</sup>, Hanbing Li<sup>5\*</sup>, Dennis Douroumis<sup>6</sup>, Lijiang Huang<sup>1\*</sup> and Huaqiong Li<sup>1,2\*</sup>

## Abstract

The primary issues in treating type 1 diabetes mellitus (T1DM) through the transplantation of healthy islets or islet  $\beta$ -cells are graft rejection and a lack of available donors. Currently, the majority of approaches use cell encapsulation technology and transplant replacement cells that can release insulin to address transplant rejection and donor shortages. However, existing encapsulation materials merely serve as carriers for islet cell growth. A new treatment approach for T1DM could be developed by creating a smart responsive material that encourages the formation of islet cell spheroids to replicate their 3D connections in vivo and controls the release of insulin aggregates. In this study, we used microfluidics to create thermally sensitive porous scaffolds made of poly(N-isopropyl acrylamide)/graphene oxide (PNIPAM/GO). The material was carefully shrunk under near-infrared light, enriched with mouse insulinoma pancreatic  $\beta$  cells ( $\beta$ -TC-6 cells), encapsulated, and cultivated to form 3D cell spheroids. The controlled contraction of the thermally responsive porous scaffold regulated insulin release from the spheroids, demonstrated using the glucose-stimulated insulin release assay (GSIS), enzyme-linked immunosorbent assay (ELISA), and immunofluorescence assay. Eventually, implantation of the spheroids into C57BL/6 N diabetic mice enhanced the therapeutic effect, potentially offering a novel approach to the management of T1DM.

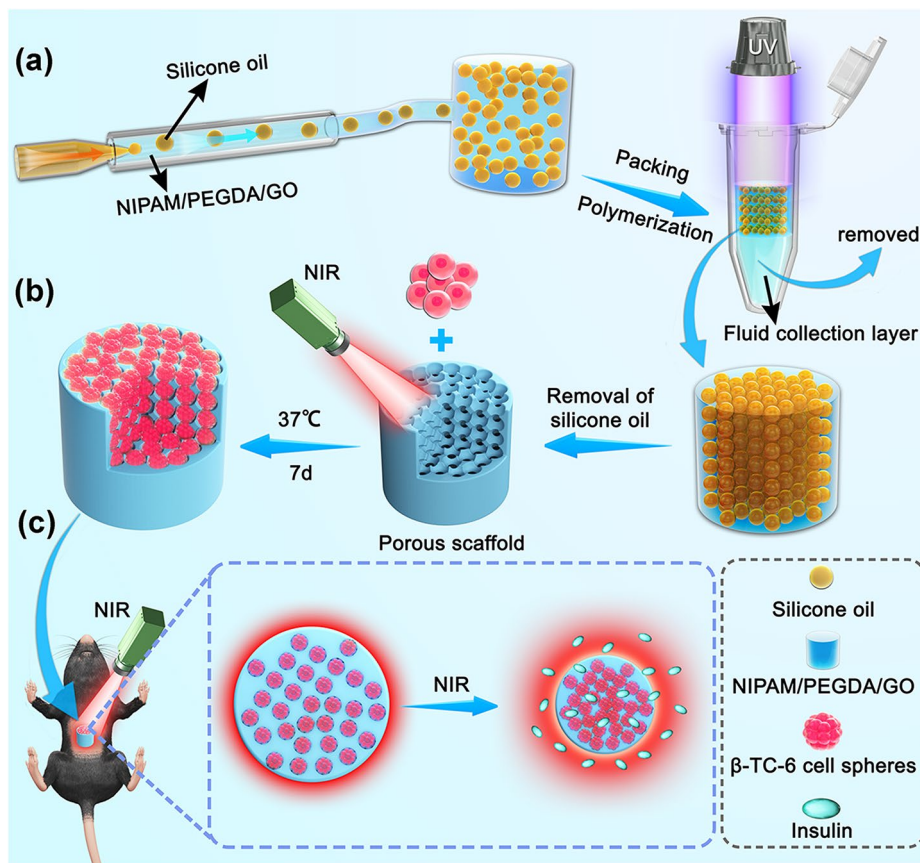
\*Correspondence:

Hanbing Li  
hanniballee@zjut.edu.cn  
Lijiang Huang  
13777030956@163.com  
Huaqiong Li  
lihq@ucas.ac.cn

Full list of author information is available at the end of the article



© The Author(s) 2024. **Open Access** This article is licensed under a Creative Commons Attribution-NonCommercial-NoDerivatives 4.0 International License, which permits any non-commercial use, sharing, distribution and reproduction in any medium or format, as long as you give appropriate credit to the original author(s) and the source, provide a link to the Creative Commons licence, and indicate if you modified the licensed material. You do not have permission under this licence to share adapted material derived from this article or parts of it. The images or other third party material in this article are included in the article's Creative Commons licence, unless indicated otherwise in a credit line to the material. If material is not included in the article's Creative Commons licence and your intended use is not permitted by statutory regulation or exceeds the permitted use, you will need to obtain permission directly from the copyright holder. To view a copy of this licence, visit <http://creativecommons.org/licenses/by-nc-nd/4.0/>.

**Graphical Abstract**

**Keywords** Type 1 diabetes mellitus, Thermally sensitive porous scaffold, Thermo-responsiveness, Controlled insulin release,  $\beta$ -TC-6 cell spheroids

**Introduction**

T1DM is an autoimmune disease caused by T-cell attacks on insulin-producing  $\beta$ -cells, reducing endogenous  $\beta$ -cell numbers and function [1]. The primary treatment for T1DM remains the administration of insulin and its analogues. This approach requires long-term injections of exogenous insulin, causing discomfort and inconvenience, as well as continuous blood glucose monitoring [2]. As T1DM, unlike type 2 diabetes (T2DM), is characterized by an absolute decline in the number of functioning  $\beta$ -cells, the regeneration and replacement of  $\beta$ -cells are of greater importance [3]. Transplantation studies in T1DM patients indicate that regenerating functional  $\beta$ -cell clusters can restore normoglycemia. Unlike insulin injections, which pose a risk of hypoglycemia, cell therapy is not harmful. However, the main challenge for cell therapy is the shortage of allogeneic transplant donors and graft inefficiency [4, 5]. Primary cultured pancreatic islets were predominantly used for islet transplantation but faced extreme donor shortages and complex islet

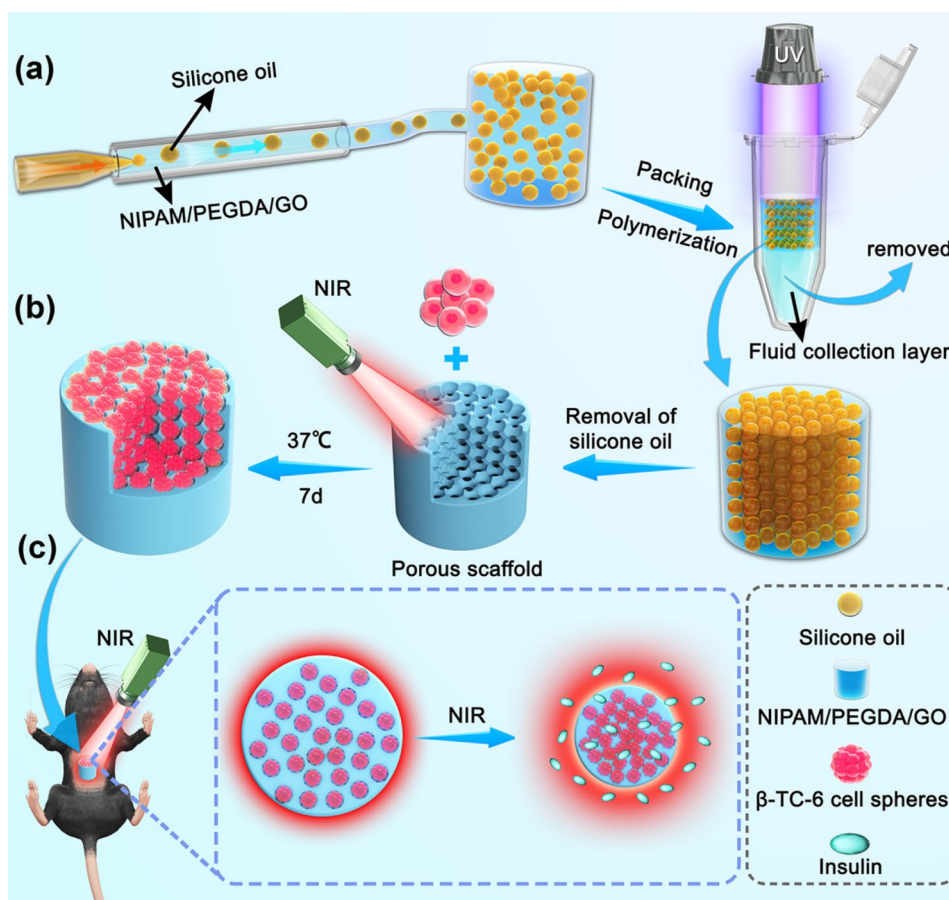
isolation techniques, making clinical demand difficult to meet [6].  $\beta$ -TC-6 cells exhibit good glucose responsiveness and insulin secretion capabilities, and they are easy to culture [7–9]. Therefore, we decided to investigate this cell line further. Furthermore, immune graft rejection, resulting in failed donor grafts, is a major issue in modern transplantation. Immunosuppressive medications are typically required during transplantation, increasing the risk of infections and other disorders by lowering immune function [10]. To mitigate the hazards associated with transplanted cells, microencapsulation technology can be used to encapsulate liquids, gases, or solids in a film, forming spherical microcapsules. This allows for the immunological isolation of allogeneic cells, avoiding host immune rejection [11, 12]. Using this technique, insulin-producing cells can thrive without immunosuppressive drugs. Bloch et al. proposed that cell microencapsulation could eliminate potentially harmful factors associated with direct cell xenografting, such as free radicals, cytokines, hypoxia, malnutrition, and specific cytotoxic

microenvironments formed during disease progression (e.g., glycototoxicity and lipotoxicity in diabetic patients) [7]. This method creates a physical barrier between the cells and the immune system. The barrier is selectively permeable, allowing smaller molecules like glucose, amino acids, oxygen, and nutrients to pass through while metabolic waste products are released. This limits the entry of immune cells and mediators, ensuring healthy engraftment and function of the islet  $\beta$ -cells [13, 14].

There are many methods for encapsulating cells via tissue engineering, and selecting a biomaterial that supports the development of islet  $\beta$ -cells is crucial. Firstly, it must act as a physical barrier. It has been reported that islet  $\beta$ -cells can grow in vivo as cell spheroids [15, 16]. We often choose substrates conducive to the production of 3D cell spheroids by these cells, as soft substrates stimulate the generation of islet  $\beta$ -cell spheroids [17, 18]. Additionally, the material must be biocompatible. Several commonly used scaffold materials, such as synthetic and natural materials like decellularized extracellular matrix hydrogels [19], alginate/methylcellulose hydrogel blends [20], polylactic acid polymer encapsulation systems [21], and polyethylene glycol hydrogel macrodevices [22], do not alter their structural morphology under tunable conditions. This suggests they only act as substrates for cell development and have no other functions. Traditional scaffolds for islet  $\beta$ -cell spheroid culture degrade too easily and can only serve as static carrier materials. Graphene oxide (GO) is an efficient photothermal conversion carbon-based nanomaterial [23] that can absorb near-infrared (NIR) laser energy to supply thermal energy for thermosensitive materials like poly(*N*-isopropylacrylamide) (PNIPAM). PNIPAM exhibits thermal responsiveness with regulated contraction and is soft enough to promote the creation of multicellular spherical structures of pancreatic  $\beta$ -cells [24, 25]. Capitano et al. demonstrated that elevating body temperature can delay or even prevent the onset of T1DM in non-obese diabetic (NOD) mice [26]. As safe and effective solutions are required to prevent and treat T1DM in humans, maintaining body temperature within physiological limits may be a viable option for future treatment [27]. Cherry's team found in 2000 and 2003 that intermittent radiation warming stimulated fibroblast growth in vitro and that intermittent radiation heating accelerated the proliferation of microvascular dermal endothelial cells [28, 29]. Transient Receptor Potential Vanilloid Receptor 2 (TRPV2), a sensor of thermal stimuli, has been reported to be activated by repeated acute thermal stress, thereby promoting angiogenesis and cell proliferation in esophageal squamous cell carcinoma (ESCC) [30]. The evidence suggests that the photothermal effect modulated by the NIR light contributes to subsequent cell proliferation. Inspired by the advantages of GO and PNIPAM, we

anticipate creating a framework with a microscopic pore size structure and dynamic stimulus response properties that can be used to build islet 3D cell spheroids and regulate molecular transport.

Here, we used microfluidics to create a porous scaffold made of PNIPAM-GO that responds to temperature by stacking microspheres generated in an oil-in-water system. The thermoresponsive shrinkage of the porous scaffold enables the development of cell spheroids through several cycles of gentle contraction, and PNIPAM, as a soft matrix, also stimulates the formation of islet  $\beta$ -cell spheroids [25, 31]. Specifically, the PNIPAM-GO porous scaffold is biocompatible and resistant to degradation. The 808 nm NIR light can be used to regulate the contraction of the scaffold to promote the production of islet  $\beta$ -cell spheroids and to regulate the release of insulin when the scaffold is used as a carrier for insulin encapsulation. Furthermore, we found that individuals with diabetes had down-regulated TRPV2 expression based on our analysis of differentially expressed genes using the GEO Big Data platform. It was also demonstrated that the pathway regulated by the differentially expressed genes was strongly associated with thermogenesis, suggesting the possibility of a novel diabetic treatment called thermotherapy. Based on our design, we used a thermally sensitive porous scaffold to grow mouse insulinoma pancreatic  $\beta$  cell ( $\beta$ -TC-6 cell) spheroids in culture, and then transplanted these spheroids subcutaneously in the abdomens of C57BL/6 N diabetic mice, where they secrete insulin in response to in vivo hyperglycemia induced by NIR light radiation (Scheme 1). The subcutaneous space is a highly desirable site for implantation due to the feasibility of subcutaneous grafting techniques, the availability of monitoring, the ability to hold large tissue bulk, and its minimally invasive properties [32, 33]. Unfortunately, limited vascularization hinders optimal implantation and induces extensive islet cell necrosis. Relevant research indicates that GO promotes angiogenesis mainly by promoting the secretion of VEGF from wound cells, which enhances the vascularization of whole skin defect wounds [34, 35]. Given the benefits mentioned above, pancreatic islet cell spheroids can be made to perform normal functions in mice for a long time. In addition, because the PNIPAM material is not easily destroyed [36], the cell spheroids it encapsulates can function for extended periods with an adequate subcutaneous blood supply, allowing them to remain in vivo for a long time. Significantly, NIR can regulate the accumulation and release of insulin stored within the scaffold in response to hyperglycemia in mice. This is achieved by varying the intensity and duration of the NIR light applied to the transplanted islet cell spheroids. In our work, we observed that four cycles of NIR light irradiation at a power of 1.5 W/cm<sup>2</sup> were beneficial in regulating insulin secretion. This novel



**Scheme 1** Methodical depiction of the entire procedure, including the production of a PNIPAM-GO thermally responsive porous scaffold, the generation of  $\beta$ -TC-6 cell spheroids, and the administration of regulated insulin to diabetic mice. **(a)** Synthesis procedure for the PNIPAM-GO thermally responsive porous scaffolds. **(b)** Formation process of  $\beta$ -TC-6 cell spheroids. **(c)** Controlled release of insulin from diabetic mice implanted with  $\beta$ -TC-6 cell spheroids

design shows promise in the treatment of T1DM due to the thermal-responsive features of the bionic PNIPAM-GO porous scaffold, its resistance to rapid degradation, and the intelligent responsive release of NIR-triggered insulin, allowing for the long-term presence of transplanted cell spheroids in vivo.

## Materials and methods

### Materials

*N,N'*-methylenebisacrylamide (Bis), poly(ethylene glycol)-block-poly(propylene glycol)-block-poly(ethylene glycol) (PEG-PPG-PEG, F108), potassium bromide (KBr), 2-hydroxy-2-methyl-1-phenylacetone (HMPP) and poly(ethylene glycol) diacrylate (PEGDA) were all acquired from Sigma-Aldrich Co., Ltd., USA. *N*-Isopropylacrylamide (NIPAM, 98%) was purchased from Macklin, Shanghai, China. *N*-Methylol acrylamide (NMAM) was purchased from Aladdin Industrial Corporation, Shanghai, China. Sodium dodecyl sulfate (SDS) was obtained from Thermo Fisher Scientific Technology Co., Ltd, China. Aqueous graphene oxide (GO) was acquired from Nanjing XFNANO Materials Tech Co., Ltd., China.

50 cs viscosity methyl silicone oil was purchased from Shin-Etsu Chemical Co., Ltd., China. Mouse insulinoma pancreatic  $\beta$ -cells ( $\beta$ -TC-6) were purchased from Shanghai Fu Heng Biotechnology Co., Ltd., China. Fetal bovine serum (FBS), Dulbecco's Modified Eagle Medium (DMEM, high sugar), and trypsin with EDTA were acquired from Gibco, USA. Calcein AM and 4',6-diamidino-2-phenylindole (DAPI) solution were obtained from Solarbio Technology Co., Ltd., China. Cell Counting Kit-8 (CCK-8) was purchased from Beyotime Biotechnology Co., Ltd., China. Bcl-2 and Bax antibody were purchased from Cell Signaling Technology Co., Ltd., USA.

### Synthesis of PNIPAM-GO thermoresponsive porous scaffold construction of a microfluidic device

A capillary glass tube with an initial inner diameter of 580  $\mu$ m was narrowed at one end using a tube puller and further refined to approximately 60  $\mu$ m using sandpaper, serving as the inner phase flow device. A capillary glass tube with an initial inner diameter of 580  $\mu$ m was employed as the outer phase flow device. AB glue was

then applied to affix a yellow needle to the slide at the entrances of both the inner and outer phases.

#### **Preparation of monodisperse microspheres**

The inner capillary phase contained methicone oil with a viscosity of 50 cs, while the outer phase comprised a mixture of NIPAM (15 wt%), GO (1 mg/mL), NMAM (1/10 of NIPAM mass ratio), SDS (2 wt%), F108 (2 wt%), HMPP (1% v/v), PEGDA (2% v/v), and Bis (1 wt%). Before use, the mixture was sonicated for 30 min and stirred for approximately an hour using a magnetic stirrer. Flow rates were set at 1 mL/h for the inner phase and 10 mL/h for the outer phase. The inner phase pump was initiated first, followed by the outer phase pump. Upon microspheres exiting the outer phase, a 2 mL centrifuge tube was used to collect the monodisperse microspheres.

#### **Porous scaffold formation**

After self-assembling into a regular cylindrical structure stacked in layers, the scaffold was exposed to ultraviolet (UV) light for approximately 20 s to cure. To create the PNIPAM-GO thermally responsive porous scaffold, the scaffold was rinsed with hexane five to six times to remove residual oil phase.

#### **Block hydrogel formation**

Block PNIPAM/GO hydrogels were synthesized by collecting an aqueous phase mixture of NIPAM (15 wt%), GO (1 mg/mL), NMAM (1/10 of NIPAM mass ratio), SDS (2 wt%), F108 (2 wt %), HMPP (1% v/v), PEGDA (2% v/v), and Bis (1 wt%) using a 2 mL centrifuge tube and curing it with UV light for 20 s.

#### **Characterizations of scaffold**

##### **Optical microscope**

A 5X magnification photo was taken.

##### **Scanning electron microscopy (SEM)**

After applying gold spray to the scaffold's surface, its surface morphology was examined using field emission scanning electron microscopy (FE-SEM, SU8010). The scaffold was placed on conductive adhesive for observation.

##### **Fourier transform infrared (FT-IR) spectroscopy**

The NIPAM monomer, GO, and PNIPAM-GO porous scaffold were dried, ground into powder, and pressed with KBr in TR mode. PEGDA was employed in the liquid film process in ATR mode. The FT-IR spectra were scanned at wavelengths of 4000 and 400  $\text{cm}^{-1}$ .

##### **Porosity**

The replacement method [37–39] was used to assess porosity. The freeze-dried scaffold was initially weighed

and recorded as  $m_1$ . Then, 4 mL of anhydrous ethanol was added, and the initial weights of the ethanol and sample were recorded as  $W_1$ . After soaking for 24 to 48 h at room temperature, the scaffold was removed, and its wet weight was measured as  $m_2$ . The amount of ethanol remaining in the sample was measured as  $W_2$ . The porosity percentage was calculated using the formula:  $\text{Porosity\%} = (m_2 - m_1)/(W_1 - W_2)$ . Three parallel samples were measured for each sample type.

#### **Degradation ratio**

Prepared scaffolds of 3 mm thickness and 10 mm diameter were collected in 2 mL centrifuge tubes, cleaned with phosphate buffered saline (PBS, Livinin), and weighed and recorded as  $W_0$  after being immersed in PBS buffer for 24 h to establish swelling equilibrium. Subsequently, the scaffolds were submerged in PBS solution for 1, 4, 7, 14, and 28 days. After removal, the surface water was blotted using filter paper, weighed, and recorded as  $W_d$ . Three batches of scaffolds were tested in triplicate. The degradation ratio (D) was calculated using the formula:  $D = (W_0 - W_d)/W_0 \times 100\%$ . D stands for degradation ratio,  $W_0$  for weight prior to degradation, and  $W_d$  for weight following degradation.

#### **Mechanical properties**

The pre-cut scaffold was shaped into cylinders with a 1 cm diameter and 2 mm thickness. During testing, samples were secured onto a metal receiver and evaluated for compression characteristics using an electronic universal material testing machine (INSTRON 5944). The scaffolds' elastic modulus was determined at a speed of 2 mm/min. Each scaffold underwent three sets of parallel tests.

#### **Photothermal analysis and thermal responsiveness shrinkage performance analysis**

##### **Photothermal properties**

The photothermal properties of various hydrogel scaffold groups were assessed under 1.5  $\text{W}/\text{cm}^2$  NIR light intensity. Thermography (FLIR) was used to measure temperature changes in the PNIPAM-GO porous scaffold under NIR irradiation at different intensities and durations.

##### **Thermal-responsive shrinkage property**

Thermography was employed to measure the volume shrinkage of the PNIPAM-GO porous scaffold at thresholds of 20 °C and 40 °C.

#### **Determination of the lower critical solution temperature (LCST)**

##### **Analysis of swelling performance**

Porous scaffolds were fabricated using various ratios of NMAM and NIPAM. After freeze-drying, the scaffolds were weighed and recorded as  $W_0$ . Subsequently, the

scaffolds were dissolved in PBS solution. (a) The mass changes resulting from different ratios of NMAM hydrophilic groups were individually noted. The weight ( $W_t$ ) of the scaffolds was measured and recorded over time. After each measurement, excess surface water was removed with filter paper. Each group of scaffolds was tested in triplicate. The swelling ratio ( $S_t$ ) was calculated using the formula:  $S_t = (W_t - W_0)/W_0 * 100\%$ . (b) Once equilibrium dissolution was achieved, mass variations due to temperature were noted for different NMAM hydrophilic group ratios and reported as  $W_T$ . The swelling ratio ( $S_T$ ) at various swelling temperatures was calculated using the formula:  $S_T = (W_T - W_0)/W_0 * 100\%$  [40].

#### **Analysis using differential scanning calorimetry (DSC)**

To calculate the LCST [41, 42], PNIPAM was dissolved in a 15 wt% aqueous solution. The test procedure was as follows: The temperature was initially reduced from room temperature to 20 °C at a cooling rate of 2 °C/min and held for 5 min. Subsequently, it was increased to 45 °C at a heating rate of 2 °C/min and maintained for 5 min. Finally, the temperature was decreased again to 20 °C at a cooling rate of 2 °C/min.

#### **Cell culture of $\beta$ -TC-6 islet cells and formation of spheroids**

$\beta$ -TC-6 islet cells were cultured in DMEM medium supplemented with 15% FBS at 37 °C with 5% CO<sub>2</sub> in a Thermo Fisher Scientific incubator. PNIPAM-GO porous scaffolds (3 mm thick, 10 mm diameter) were sterilized under UV light for over 4 h, followed by sequential washes with 75% ethanol (twice), 50% ethanol (twice), PBS (four times), and DMEM (once or twice). To construct  $\beta$ -TC-6 islet cell spheroids, each scaffold was coated with 50  $\mu$ L of cell suspension at a density of  $2 \times 10^6$  cells/mL, followed by slow addition of 400  $\mu$ L of culture media. After cell seeding, scaffolds underwent five cycles of NIR radiation at 1.25 W/cm<sup>2</sup>, each cycle lasting approximately 60 s with 60-second intervals. The medium was refreshed daily with 250  $\mu$ L, maintaining a total culture volume of 450  $\mu$ L. After spheroid formation, cells were stained with 5  $\mu$ M Calcein AM and 5  $\mu$ g/mL DAPI for observation.

#### **Quantitative real-time PCR (qPCR) assay**

The steps of quantitative real-time PCR were as previously described [43]. All primer information is listed in Tab. S1.

#### **In vitro cytocompatibility assays**

##### **Extraction of scaffold leachate**

The sterilized scaffold was immersed in 1.256 mL of DMEM medium and placed in the incubator at 37 °C for 48 h. Subsequently, the leachate was collected and stored at 4 °C.

#### **Cytotoxicity assay**

Cells were seeded in 96-well plates and incubated for 1 day before replacing the medium with scaffold leachate every 2 days. Cytotoxicity was assessed on days 1, 3, 5, and 7 using the enhanced CCK-8 kit, and absorbance at 450 nm was measured with a microplate reader.

#### **In vitro insulin secretion function assays**

##### **Enzyme-linked immunosorbent assay (ELISA)**

**Sample Preparation** For the in vitro insulin secretion assay,  $\beta$ -TC-6 cells were digested and seeded in 24-well culture plates at a density of 100,000 cells per well. The plates were then incubated at 37 °C in a 5% CO<sub>2</sub> incubator for 48 h. The cells were washed 2–3 times with PBS buffer followed by 2–3 washes with 1 mL of sugar-free Krebs-Ringer Bicarbonate HEPES (KRBH, JingKeHuaXue) buffer containing 0.1% Bovine Serum Albumin (BSA, Biosharp). After incubating at 37 °C in a 5% CO<sub>2</sub> incubator for 1 h, each well was exposed to 500  $\mu$ L of either 1.38 mM or 11.1 mM glucose solution for 30 min, according to experimental conditions. NIR light irradiation at 1.5 W/cm<sup>2</sup> was applied for 4 cycles (30 s per cycle with a 60-second interval, reaching a maximum temperature of approximately 41 °C). Supernatants were collected from the experimental group after NIR illumination and directly from the control group. For determination of insulin secretion in vivo, mouse plasma samples were obtained, and whole blood was anticoagulated with heparin or EDTA, mixed, and kept on ice. Plasma was collected by centrifugation at 4 °C at 1000–2000 g for 10 min to obtain the yellow or light yellow supernatant.

**Insulin measurement** Insulin levels in the supernatant or blood were quantified using a Mouse Insulin ELISA Kit (Ultrasensitive, Beyotime). Following the manufacturer's protocol, the test sample, enzyme-labeled antibody, color development solution, and termination solution were sequentially added to a 96-well plate. After completing the final mixing step, A450 values were measured using a microplate reader.

##### **Fluorescence immunoassay**

To visualize the distribution of residual insulin in the porous scaffold following insulin secretion, samples were fixed in 4% paraformaldehyde for 30 min and washed three times with PBS for 5 min each. Subsequently, samples were permeabilized with 0.1% Triton X-100 for 15 min and washed three times with PBS for 5 min each. Samples were then blocked with 5% BSA for 1 h, followed by aspiration of residual BSA. Rabbit anti-insulin primary antibody (C27C9) (1:100) was added and incubated overnight at 4 °C, followed by washing three times with PBS for 5 min each. Samples were then incubated with goat anti-rabbit secondary antibody (1:100) for 1 h at room

temperature in the dark, followed by four washes with PBS. Finally, ready-to-use DAPI was added, incubated for 10 min at room temperature in the dark, and washed three times with PBS. The treated samples were imaged using a confocal microscope.

### **In vivo biosafety evaluation**

The Ethics Committee of the Wenzhou Institute of the Chinese Academy of Sciences approved the use of animal experimentation (WIUCAS 20033115, 20200331). For this study, 40 C57BL/6 N male mice were used in 4-week in vivo safety studies, during which their well-being and survival were carefully monitored.

### **General physical indicators**

We employed a photographic recording method using a smartphone camera app to document the weight, activity, and wound healing progress of mice over several weeks.

### **Serum biochemical indicators**

Aspartate aminotransferase (AST), alanine aminotransferase (ALT), blood urea nitrogen (BUN), creatinine (CR), tumor necrosis factor- $\alpha$  (TNF- $\alpha$ ), and interleukin-4 (IL-4) inflammatory factors were quantified using respective assay kits, and their levels were determined using a microplate reader.

### **Organ morphological changes**

Major mouse organs including the heart, liver, spleen, and lung were excised, fixed in 4% formaldehyde for 24 h, sectioned into frozen slices, and stained with Hematoxylin-Eosin (HE). Light microscopy was used to observe the stained sections and capture images.

### **In vivo evaluation of treatment effects in diabetic mice**

#### **Procedures for inducing diabetes in mice**

**Preparation of sodium citrate buffer:** A 0.1 M solution of sodium citrate and 0.1 M citric acid were mixed in a ratio of 28:22 to achieve a final pH of 4.2–4.5 (approximately 4.4). The solution was then filtered using a 0.22  $\mu$ m needle filter (Thermo Scientific) to remove bacteria.

**Modeling and confirmation process** We weighed 20 mg of streptozotocin (STZ) and prepared a buffer at a concentration of 5 mg/mL. The cooled buffer was added to STZ, vortexed until clarified, and injected intraperitoneally at 10  $\mu$ L/g. Control mice received an equivalent volume of buffer. Injections were administered daily for 5 consecutive days, and fasting blood glucose levels were measured 7 days after the final injection. Successful modeling was defined as achieving fasting blood glucose levels exceeding 250 mg/dL.

### **Intraperitoneal glucose tolerance test (IPGTT)**

Mice were fasted overnight and then injected intraperitoneally with a glucose solution (2 g/kg body weight) the following day. Blood glucose levels were monitored at regular intervals (0, 30, 60, 90, and 120 min) after injection.

### **Evaluation of treatment effects**

We evaluated the therapeutic effects of  $\beta$ -TC-6 cell spheroid transplantation in diabetic mice based on changes in blood glucose and body weight. To detect insulin secretion in mice post in vivo transplantation, we removed the skin at the transplant site, sectioned the subcutaneous tissue (including blood vessels) into paraffin tissue sections, performed antigen retrieval using a microwave repair method, and followed the remaining steps of the insulin detection procedure similar to the aforementioned *in vitro* immunofluorescence detection method. Goat anti-Rabbit IgG (H+L) Highly Cross-Adsorbed Secondary Antibody (Alexa Fluor Plus 594, ThermoFisher) was used for direct detection of the CD31 index, a marker of angiogenic proliferation at the graft sites.

### **Bioinformatics analysis**

We utilized the GSE29221 dataset from the GEO database (<https://www.ncbi.nlm.nih.gov/geo/>) in MINiML format. mRNA differential expression was assessed using the limma package in R software (version 3.40.2). Adjusted P values were calculated in GEO to correct for false positives, with “Adjusted  $P < 0.05$  and  $|\log_2(\text{fold change})| > 1$ ” as the threshold for differential expression screening. For functional enrichment analysis, gene ontology (GO) was employed to annotate genes by molecular functions (MF), biological pathways (BP), and cellular components (CC). KEGG pathway analysis provided insights into gene functions and higher-level genomic functional information. Genes associated with thermogenesis were retrieved from the Genecards database (<https://www.genecards.org/>). Venn diagrams and heatmaps were generated using <https://www.bioinformatics.com.cn> (last accessed on 20 Feb 2024), an online platform for data analysis and visualization.

### **Statistical analysis**

Each experiment was conducted at least three times, and statistical analyses were performed using Graphpad Prism 8 software. For the comparison of two groups, statistical analysis was performed using Student's t-test. Additionally, one-way or two-way ANOVA was performed using Bonferroni's multiple comparison test to compare more than two groups. Statistical significance was defined as  $p \leq 0.05$ , with \* indicating  $p \leq 0.05$ , \*\* indicating  $p \leq 0.01$ , \*\*\* indicating  $p \leq 0.001$  and \*\*\*\* indicating  $p \leq 0.0001$ ; “ns” denotes no statistically significant difference.

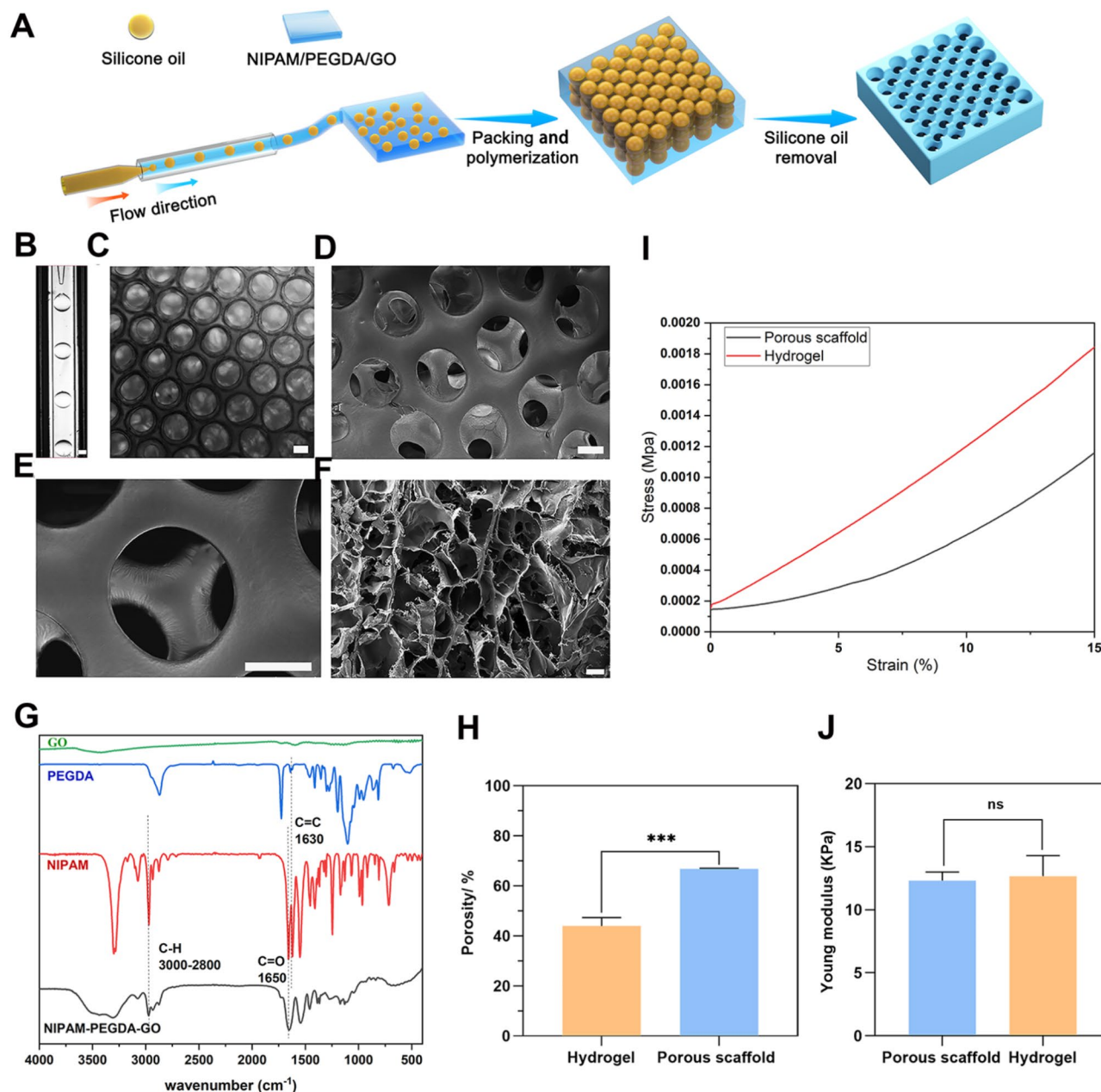


**Fig. 1** Characterization of the PNIPAM-GO porous scaffold. **(A)** Diagram illustrating the manufacturing process. **(B)** Light microscopy image showing the oil-in-water microspheres produced by the microfluidic device. **(C)** Light microscopy image. **(D)** Scanning electron microscopy (SEM) image. **(E)** SEM image showing local magnification of a single pore. **(F)** SEM image showing the PNIPAM-GO bulk hydrogel. **(G)** Fourier transform infrared spectroscopy analysis. **(H)** Porosity assessment. **(I, J)** Mechanical properties testing. Mean  $\pm$  SD ( $n=3$ ). (\*\*\*:  $p < 0.001$ , ns: non-significant). Scale bar, 100  $\mu\text{m}$  (B, C, D, E, F)

## Results and discussion

### Synthesis and characterization of PNIPAM-GO porous scaffolds

Figure 1A depicts the overall processes for synthesizing the PNIPAM-GO porous scaffold. To create the dense stack of oil-in-water microspheres depicted in Fig. 1B, methyl silicone oil with a viscosity of 50 cs served as the oil phase, while the mixed solution of NIPAM, GO, and PEGDA was employed as the aqueous phase. The

mixture underwent UV curing, and the oil phase was subsequently removed using hexane to produce the porous scaffold (Fig. 1C). The scaffold exhibited a porous structure with uniformly sized pores around 200  $\mu\text{m}$  and a regular arrangement. After dehydration and lyophilization, we examined the porous scaffolds under SEM, revealing interoperable small pores with dimensions in the tens of micrometers range (Fig. 1D and E). These scaffolds exhibited uniformly sized surface pore

structures and interconnected micropore networks, facilitating the transport of cellular oxygen and nutrients, which is beneficial for the growth of islet cells [44–46]. In contrast, the block *PNIPAM*/GO hydrogel exhibited irregular pore sizes and shapes (Fig. 1F). The *PNIPAM*-GO FT-IR spectra are depicted in Fig. 1G, where PEGDA was found to facilitate the cross-linking of NIPAM [47]. The =C-H peaks of NIPAM and PEGDA are situated between 3000 and 2800  $\text{cm}^{-1}$ . The porous scaffold constitutes a *PNIPAM*-GO complex, indicating polymerization of the NIPAM monomer into *PNIPAM*, as evidenced by the significant weakening of the =C-H hydrogen absorption peak at 3000  $\text{cm}^{-1}$ , the -C=O stretching vibration absorption peaks of NIPAM at approximately 1650–1630  $\text{cm}^{-1}$ , and the C=C double bond [48, 49]. Figure 1H illustrates the porosity of the *PNIPAM*-GO scaffold estimated at approximately 70%, significantly higher than the block gel scaffold's porosity of 40% ( $p < 0.001$ ). The latter scaffold exhibited superior penetration, thereby enhancing nutrient and oxygen transfer to the cells and promoting their survival [50]. Figure 1I and J depict the mechanical characteristics of the scaffolds. The Young's modulus of the porous and bulk scaffolds showed no significant difference, measuring 12.31 KPa and 12.67 KPa respectively, indicating that the synthesized porous scaffolds retain mechanical properties comparable to those of the bulk scaffolds. Additionally, *PNIPAM*, known for its soft matrix, was found to facilitate the development of islet cell spheroids with a Young's modulus of approximately 10 KPa [18]. Considering the results of scaffold degradation in PBS, DMEM, and simulated body fluids (SBF) (Fig. S1), the overall degradation rate of this photothermal material does not exceed 5% for both porous and block scaffolds. These findings suggest that the *PNIPAM*/GO scaffolds exhibit a low degradation rate, which is beneficial for the long-term therapeutic efficacy of islet cell spheroids.

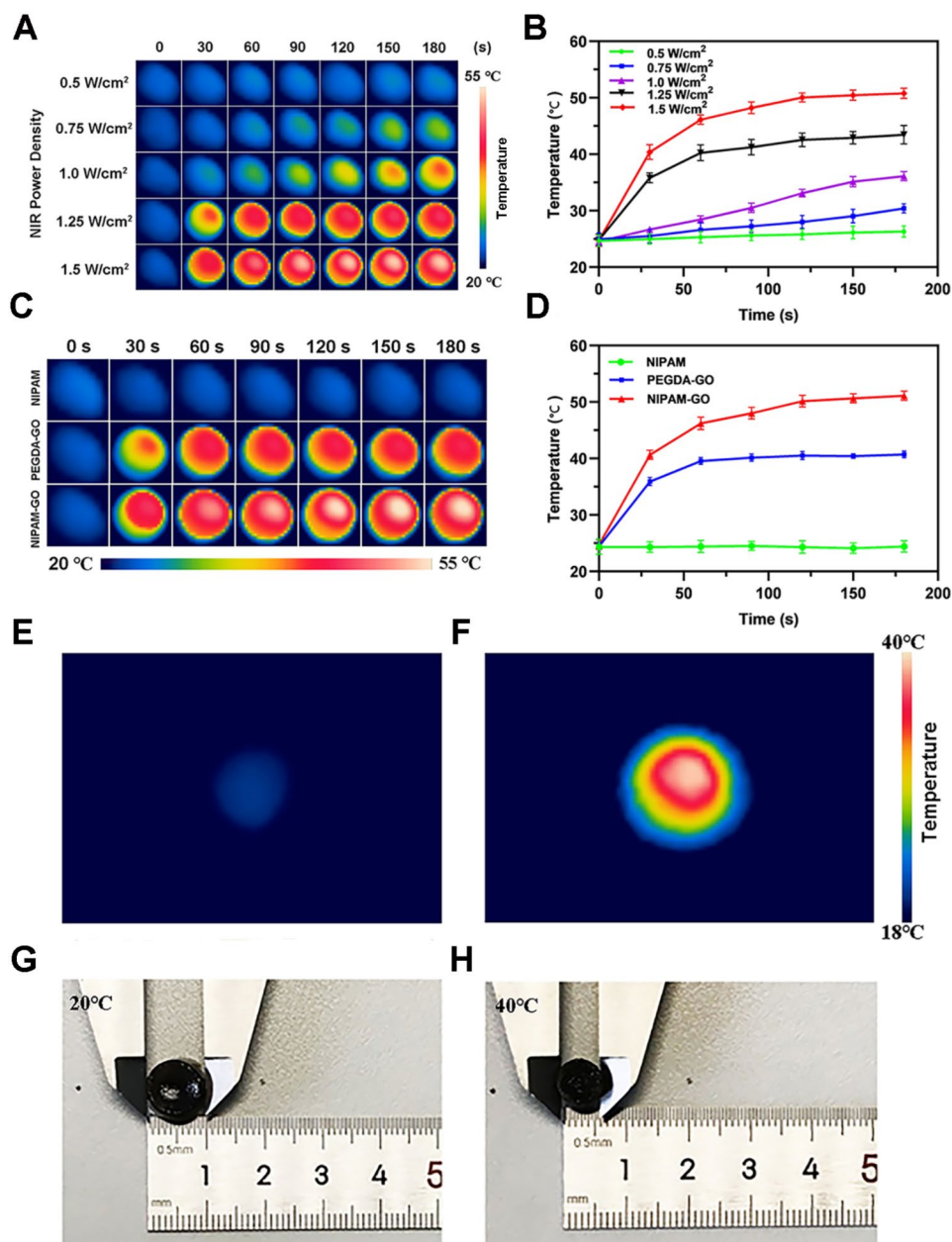
#### Thermo-responsive shrinkage performance and photothermal efficiency

Figure 2A and B present the findings of the *PNIPAM*-GO thermally responsive porous scaffold for various power variations over time in photothermal maps. At ambient temperature, NIR light power below 1.25  $\text{W}/\text{cm}^2$  results in a temperature below 35 °C within 3 min. With NIR power set to 1.25  $\text{W}/\text{cm}^2$ , the temperature reaches 40 °C within 3 min. Increasing the NIR power to 1.5  $\text{W}/\text{cm}^2$  achieves temperatures of 40 °C within 30 s and 50 °C within 3 min. Figure 2C and D display the photothermal performance results of the *PNIPAM*-GO scaffold compared to the control groups: PEGDA-GO scaffold without NIPAM and *PNIPAM* scaffold without GO, over time. Observations show that the *PNIPAM* scaffold's temperature remained stable at room temperature, whereas the

PEGDA-GO scaffold did not reach 40 °C within 3 min. In contrast, the *PNIPAM*-GO scaffold reached 40 °C within 30 s. In conclusion, these findings demonstrate that GO serves as the primary scaffold for photothermal performance, and *PNIPAM*-GO enhances GO's photothermal performance. Figure 2E and F depict a thermally sensitive porous scaffold using *PNIPAM*-GO as the primary hybrid system, exposed to NIR radiation at a power of 1.5  $\text{W}/\text{cm}^2$ . Figure 2G and H show the scaffold shrinking from a diameter of 1 cm to 0.55 cm, at a shrinkage rate of approximately 45%, due to the temperature increase (20–40 °C). Movie S1 depicts the contraction process.

#### Characterization of low critical volume phase transition temperature

Swelling performance tests [51] and differential scanning thermal (DSC) [52] were conducted to evaluate the thermal responsiveness of *PNIPAM*-GO porous scaffolds below their lower critical solution temperature (LCST). A hydrophilic group known as N-Hydroxymethylacrylamide (NMAM) [53] can modify the scaffold's LCST. Figure 3A shows that the scaffold's swelling ratio increases linearly from 2 min to 30 min upon addition of different ratios of NMAM (NMAM=0, 1:10, 1:5, 1:2) over a 24-hour period. Due to the porous structure of the scaffold, it can absorb water and rapidly expand to reach swelling equilibrium. Figure 3C demonstrates that the addition of NMAM hydrophilic groups at various ratios enhances the final swelling ratio. According to the phase transition theory of hydrogels [54, 55], hydrogels are soluble in water below the LCST because hydrogen bonds form between water molecules and hydrophilic groups. However, with increasing temperature, hydrogen bonding decreases while hydrophobic interactions increase, leading to molecular chain contraction and gel formation due to physical entanglement. The maximum hydrogen bonding of hydrogels occurs as temperature decreases, approximated by the DSC melting endothermic peak (i.e.,  $T_{\text{DSC, peak}}$ ), which corresponds to the scaffold's LCST. Therefore, DSC measurements can estimate the LCST of hydrogels, consistent with prior research [52, 54, 55]. Figure 3B shows the results of temperature-dependent swelling performance tests with different NMAM ratios added to the scaffold, revealing that the swelling ratio of pure *PNIPAM* declines sharply at around 32 °C, indicating its LCST is approximately 32 °C. The LCSTs of NMAM: NIPAM=1:2, 1:5, and 1:10 are approximately 45 °C, 42 °C, and 40 °C, respectively. Therefore, these results suggest that NMAM can be added to the scaffold to increase its LCST. Thus, we selected NMAM=1:10 for subsequent spheroid formation and insulin-controlled release experiments because it met the following criteria: (a) a temperature environment slightly above body temperature (around 40 °C) and (b) reduced scaffold



**Fig. 2** Photothermal characterization and thermal responsiveness characterization of porous scaffolds using PNIPAM and GO as the main hybrid system. (A) Photothermal representation of NIR laser irradiation with varying power over time. (B) Data presentation for A. (C) Photothermal plots of PNIPAM-GO mixed group, PEGDA-GO group, and PNIPAM group scaffolds under constant NIR irradiation ( $1.5 \text{ W/cm}^2$ , 0–180 s). (D) Data presentation for C. Photothermal map of PNIPAM-GO mixed scaffold at (E)  $20 \text{ }^\circ\text{C}$  and (F)  $40 \text{ }^\circ\text{C}$ . Volume size changes at (G)  $20 \text{ }^\circ\text{C}$  and (H)  $40 \text{ }^\circ\text{C}$ . Mean  $\pm$  SD ( $n=3$ )

shrinkage with the addition of NMAM [53]. Based on our findings (Fig. 3B) and published work, the LCST of pure PNIPAM is approximately  $32 \text{ }^\circ\text{C}$  [56–58]. Figure 3D shows that adding NMAM to the porous scaffold increases the LCST to  $40.8 \text{ }^\circ\text{C}$  at NMAM=1:10.

### Spheroids encapsulation

In this investigation, the cytocompatibility of the fabricated scaffolds was assessed by culturing  $\beta$ -TC-6 cells in porous scaffolds immersed for 48 h without NIR light

irradiation or with NIR light irradiation for 5 cycles (Fig. 4A). A CCK-8 assay was used to assess cytotoxicity on days 1, 3, 5, and 7 (Fig. 4B). The findings suggested that the PNIPAM-GO porous scaffold can be used to encapsulate  $\beta$ -TC-6 cells, as there was no significant difference between the NIR-irradiated and non-irradiated scaffolds on days 1, 3, 5, and 7 compared to the control group. NIR light has been reported to control the contraction of thermally responsive scaffolds and thereby stimulate the production of cell spheroids [31, 59]. When

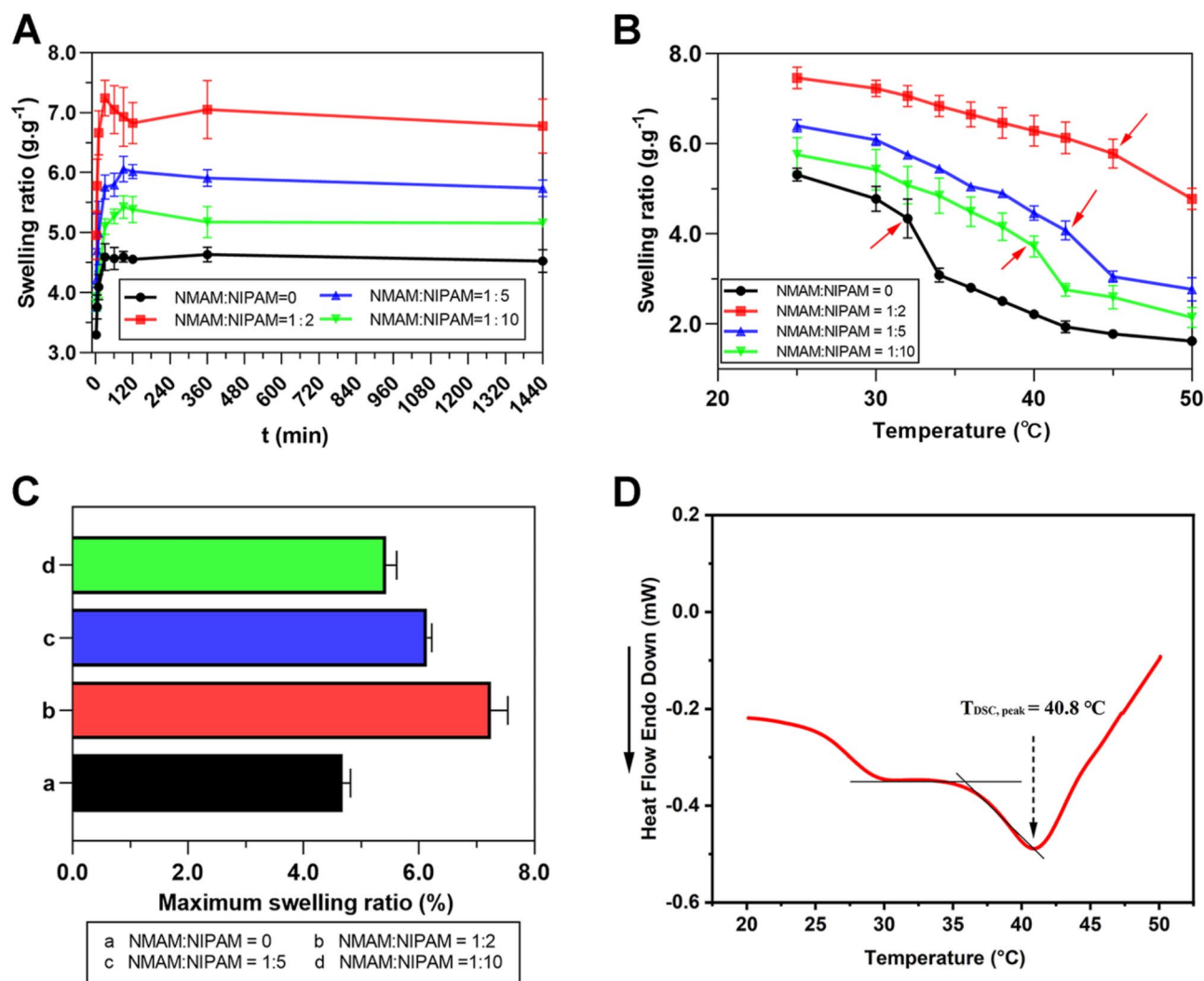


**Fig. 3** The characterization of LCST includes the swelling performance test and DSC analysis of the scaffold (NIPAM and NMAM as the main hybrid system). **(A)** Swelling property variations over time for various NMAM ratios added to NIPAM scaffolds. **(B)** Swelling property variations with temperature for various NMAM ratios added to NIPAM scaffolds to determine LCST. Red arrows indicate the LCST values for different NMAM proportions. **(C)** Maximum swelling ratio for various NMAM ratios added to NIPAM scaffolds. Mean  $\pm$  SD ( $n=3$ ). (\*:  $p < 0.05$ , \*\*:  $p < 0.01$ , \*\*\*:  $p < 0.001$ , \*\*\*\*:  $p < 0.0001$ ). **(D)** DSC characterization of LCST values for PNIPAM solutions with NMAM : NIPAM = 1:10

the scaffold shrinks, the cells can uniformly press into the pores while the culture medium is expelled, which is analogous to natural fish predation. This process encourages the development of cell spheroids by facilitating cell aggregation in the pores. We investigated the principle of cell spheroid creation by varying the number of NIR irradiation cycles and days, as illustrated in Fig. 4C. The results for the pattern of NIR light irradiation cycles on cell spheroid creation, as shown in Fig. S2, revealed that 5 cycles of NIR irradiation can be used to encapsulate the cells and create cell spheroids. According to confocal image analysis, as shown in Fig. 4D and E, cells began to form spheroids on days 1 and 4 following 5 cycles of NIR irradiation, though the spheroids were less concentrated. In contrast, on days 7 and 14, as depicted in Fig. 4F and

G, the cells formed dense clusters resembling islet-like cell spheroids [60] after 5 cycles of NIR light irradiation. Fig. S3 depicts the 3D structure of the cell spheroids as captured by confocal microscopy. Therefore, it was morphologically determined that the cell spheroids cultivated for less than 7 days in PNIPAM-GO thermo-responsive porous scaffolds can be utilized for further investigation. In addition, we performed quantitative cellular analysis of mouse islet cell spheroids, and their growth trends were consistent with the immunofluorescence results (Fig. S4).

#### Glucose-stimulated insulin release

This study employed  $\beta$ -TC-6 cell spheroids to investigate glucose-stimulated insulin release (GSIS) and examined the impact of a thermo-responsive porous scaffold

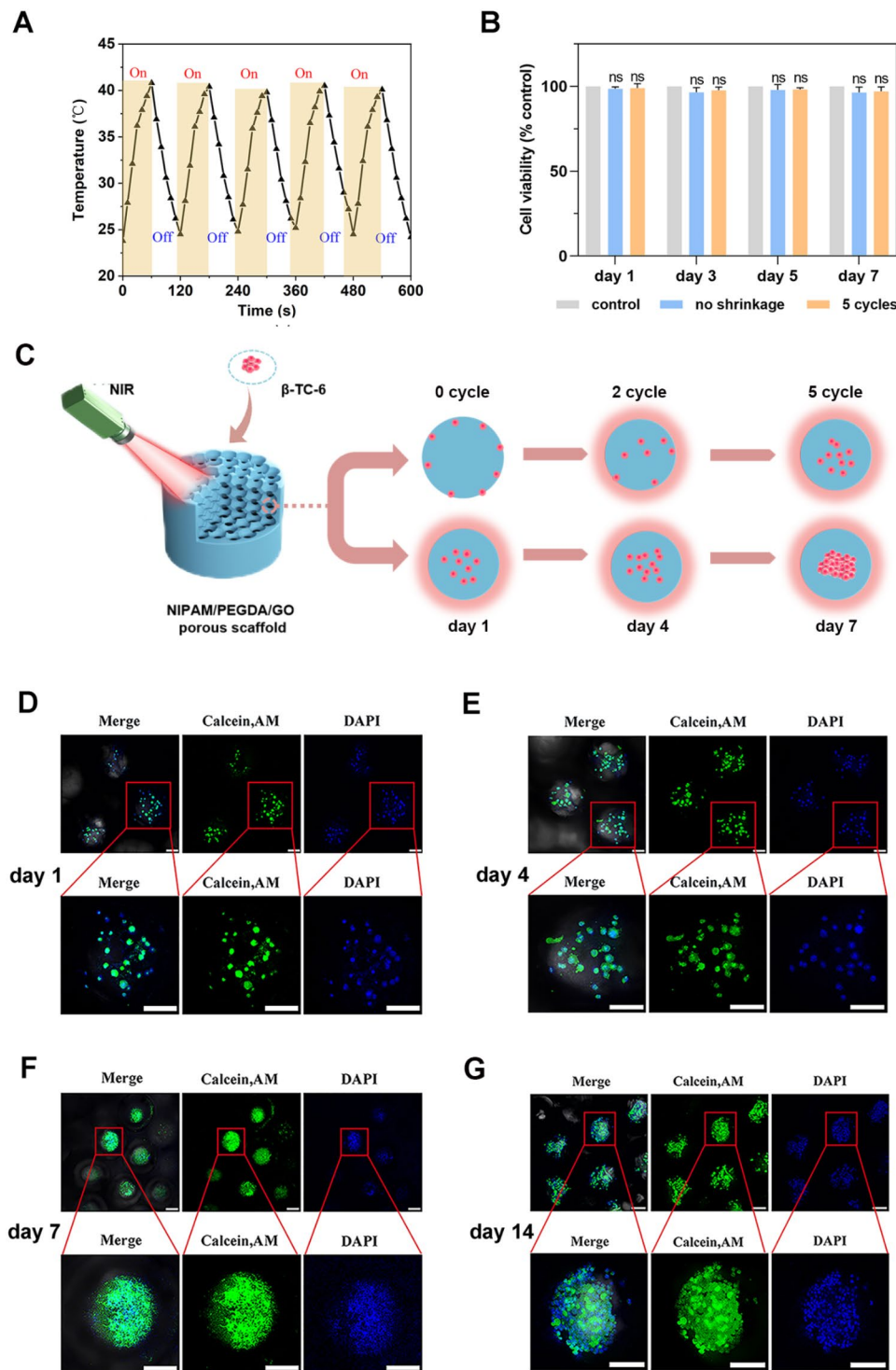


**Fig. 4**  $\beta$ -TC-6 cell spheroid encapsulation. **(A)** Time (t) vs. temperature (T) plot during 5 cycles of NIR illumination. **(B)** Cytotoxicity experiments on days 1, 3, 5, and 7 for groups exposed to and not exposed to NIR radiation. **(C)** Illustration of the formation pattern of  $\beta$ -TC-6 cell spheroids with varying numbers of cycles and days of NIR irradiation. Confocal images of  $\beta$ -TC-6 cells on days **(D)** 1, **(E)** 3, **(F)** 5 and **(G)** 7 following 5 cycles of NIR irradiation with Calcein, AM (green), and DAPI (blue). Mean  $\pm$  SD ( $n=4$ ). (ns: non-significant). Scale bar, 100  $\mu$ m in (D, E, F, G)

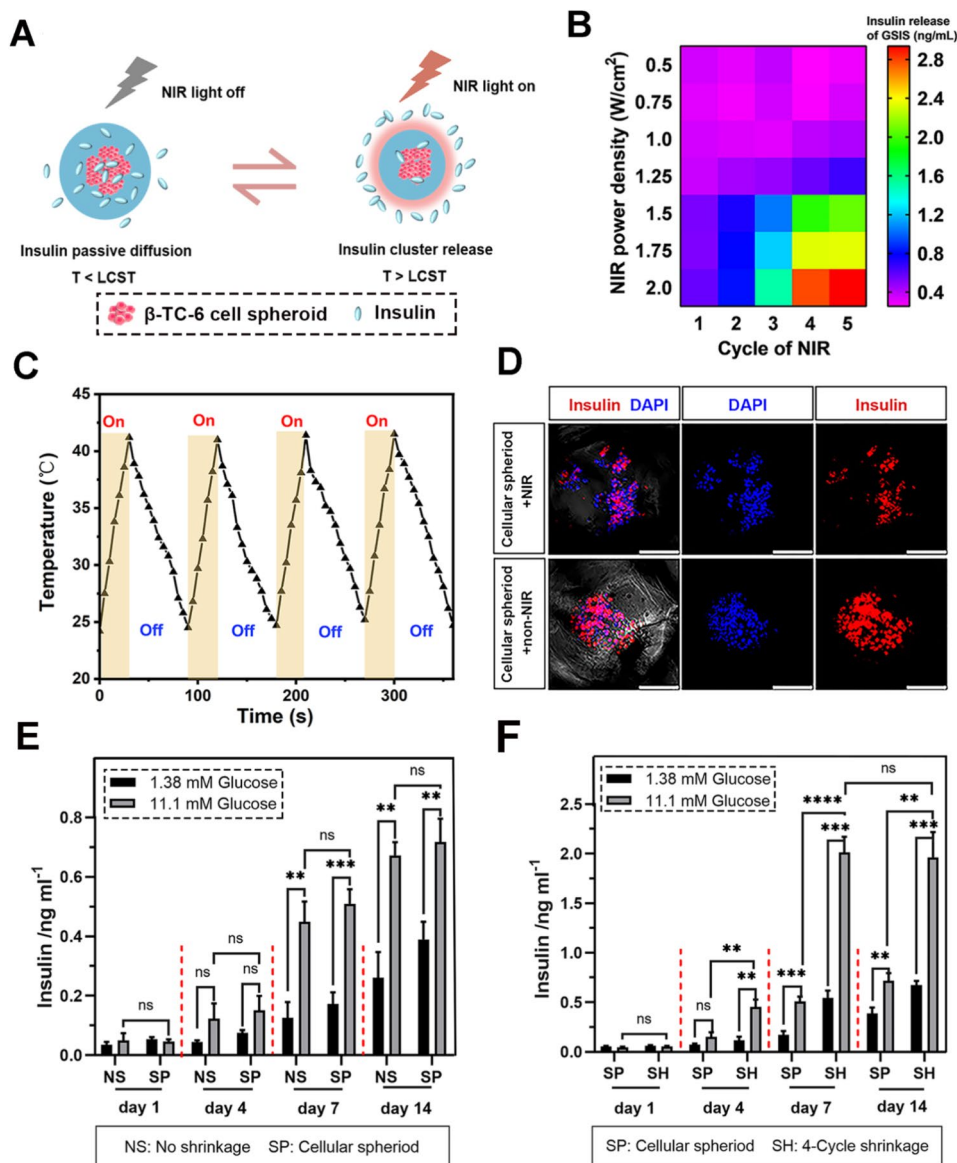


**Fig. 5** Insulin secretion from thermally responsive porous scaffold-encapsulated  $\beta$ -TC-6 cells under NIR control. **(A)** A schematic illustration of NIR light regulation of insulin release from  $\beta$ -TC-6 cell spheroids. **(B)** Investigating insulin release experiments with different NIR light irradiation power and number of cycles. **(C)** Time-temperature variation plots of 4 cycles of NIR light irradiation to control insulin release (power: 1.5 W/cm<sup>2</sup>, 30 s irradiation per cycle, 60 s interval). **(D)** Immunofluorescence plots of porous scaffolds encapsulating  $\beta$ -TC-6 cells with and without NIR irradiation to control insulin release, with red and blue fluorescence representing insulin and nucleus, respectively (Scale bar, 100  $\mu$ m). **(E)** Graphs depict the effects of omitting NIR light from GSIS tests designed to regulate insulin secretion. **(F)** Graph showing the findings of the GSIS insulin release experiment using NIR light. (NS: no NIR light when the porous scaffold encapsulates cells; SP: cell spheroids created by 5 cycles of NIR light (1.25 W/cm<sup>2</sup>) irradiation when the porous scaffold encapsulates cells; SH: Cell spheroids' controlled insulin secretion after being exposed to NIR light (1.5 W/cm<sup>2</sup>) for 4 cycles). Mean  $\pm$  SD ( $n=3$ ). (ns: non-significant, \*\*,  $p < 0.01$ , \*\*\*,  $p < 0.001$ , \*\*\*\*,  $p < 0.0001$ )

composed of PNIPAM-GO on regulated insulin release. PNIPAM is known to be a thermally sensitive shrinking material, releasing the loaded drug by rapid contraction when the temperature exceeds the LCST of the scaffold, while passive diffusion is the primary mechanism when the temperature is below the LCST. When the temperature approaches the LCST, the drug is trapped within the scaffold, preventing its release. Thus, insulin

can be delivered using NIR light to control its release from a porous scaffold [61, 62]. Figure 5A depicts the regulation of insulin release from  $\beta$ -TC-6 cell spheroids by NIR light. Our insulin secretion experiments, using static glucose stimulation of  $\beta$ -TC-6 cells, showed a significant difference in insulin secretion between 11.1 mM glucose as the stimulated glucose concentration and 1.38 mM glucose as the control glucose concentration,

with a 30-minute stimulation period (Fig. S5). As shown in Fig. 5B, we also investigated the effects of NIR light intensity and the duration between treatments on insulin secretion. Subsequently, NIR light irradiation at 1.5 W/cm<sup>2</sup> for 4 cycles was found to be effective in controlling insulin release, with a peak temperature of approximately 41 °C, exceeding the LCST. The NIR irradiation cycle is depicted in Fig. 5C, and the immunofluorescence plot in Fig. 5D demonstrates that, following four cycles of NIR irradiation to regulate insulin release, the amount of insulin in the scaffold decreased. These findings suggest that NIR illumination can regulate the release of insulin from the scaffold's pores. Quantitative analysis of GSIS utilizes an enzyme-linked immunosorbent assay (ELISA) test. Figure 5E illustrates the division of multicellular spheroids of  $\beta$ -TC-6, created by five cycles of NIR light (1.25 W/cm<sup>2</sup>), and structures formed by cells growing in a ring around the scaffold wall (Fig. S2), into two groups for GSIS tests without NIR light regulation of insulin release. For cell spheroids without NIR-controlled release and for cells growing along the wall, there was no discernible difference in insulin release between days 1 and 14. On days 7 and 14, the differences between stimulated and unstimulated blood glucose levels were significant. There was a progressive increase in insulin release from days 1 through 14, with a slower increase after day 7, resulting in less than 0.8 ng/mL of insulin release in response to stimulated glucose concentrations on days 7 and 14. In Fig. 5F, multicellular spheroids of  $\beta$ -TC-6 generated by 5 cycles of NIR light (1.25 W/cm<sup>2</sup>) were divided into two groups: (a) those not irradiated with NIR light during insulin release, and (b) those exposed to NIR light (1.5 W/cm<sup>2</sup>) to control release. In contrast to cell spheroids without NIR irradiation, insulin release was significantly higher in the NIR-controlled cell spheroids from days 4 to 14. There was a gradual increase in insulin release for the group exposed to NIR light from days 1 through 14, while there was no discernible difference between the insulin release from GSIS on days 7 and 14. The insulin release reached 2.0 ng/mL. This insulin secretion may provide a reference point for the therapeutic effect in diabetic mice when combined with the therapeutic effect of insulin in mice [63, 64]. Furthermore, we verified that the treatment did not promote apoptosis by detecting the apoptosis-promoting protein Bax and the apoptosis-inhibiting protein Bcl-2 (Fig. S6). The effectiveness of the treatment was sufficiently demonstrated.

#### **In vivo biosafety evaluation**

For the in vivo safety tests, male C57BL/6 N mice were transplanted and monitored over a 4-week period. The mice gained weight evenly (Fig. S7) after receiving the PNIPAM-GO porous scaffold subcutaneously in the abdomen, with no noticeable difference between the

control groups. Growth activity of the mice was normal on the 28th postoperative day (Movie S2). Faint suture traces were visible, and the wounds were nearly fully healed without infections observed (Fig. S8). On the 28th day, all mice were euthanized, and major organs (heart, liver, spleen, and kidney) were removed for morphological examination of tissue Sect. [65]. Figure 6A illustrates no apparent abnormalities in organ comparison between the scaffold-transplanted group and normal mice. Mice euthanized on days 3, 7, 14, and 28 had blood collected from the abdominal aorta, which was then centrifuged to obtain serum for biochemical analysis, including measurements of aspartate aminotransferase (AST), alanine aminotransferase (ALT), urea nitrogen (BUN), and creatinine (CR) [65, 66]. Figure 6B and C show the assessment of liver function by ALT and AST levels. Figure 6D and E show the BUN and Cr levels for the assessment of kidney function. Figure 6F and G show the measurements of TNF- $\alpha$  and IL-4 inflammatory factor levels in the serum of mice to assess the degree of inflammation. These findings indicate no inflammatory reactions and no significant differences in liver and kidney function between the PNIPAM/GO scaffold transplantation group and normal mice. This suggests that the developed scaffolds are safe to utilize as a cell carrier in cell transplantation therapy.

#### **Control of blood glucose in diabetic mice: an in vivo study**

The PNIPAM-GO porous scaffold demonstrated favorable biosafety and biocompatibility with  $\beta$ -TC-6 islet cells in the in vivo transplantation study. The subcutaneous space is a highly desirable site for implantation due to its ability to accommodate large tissue volumes and its minimally invasive nature, as well as its accessibility to NIR light [33, 67]. However, transplantation encountered challenges including limited vascularization of subcutaneous tissue, oxygenation issues, and foreign body reactions associated with cell transplantation [32]. Previous studies have demonstrated that GO can enhance VEGF production [68]. Expression levels of hypoxia-inducible factor HIF-1 $\alpha$  and pro-angiogenic factor VEGF increased at the graft site in mice implanted with PNIPAM/GO scaffolds subcutaneously in the abdomen for 4 weeks (Fig. 7A and B). HE tissue staining revealed numerous erythrocyte-containing blood vessels capable of delivering oxygen to the implanted cells (Fig. 7C). Immunofluorescent staining of CD31 further confirmed the presence of numerous blood vessels (Fig. 7D). The microencapsulated porous scaffold developed for cell encapsulation mitigated foreign body reactions. Four weeks post-implantation of microencapsulated cell spheroids in abdominal subcutaneous tissues, the mRNA expression level of  $\alpha$ -smooth muscle actin ( $\alpha$ -SMA) was consistent with that of the normal group, indicating absence of fibrotic reaction due to cell

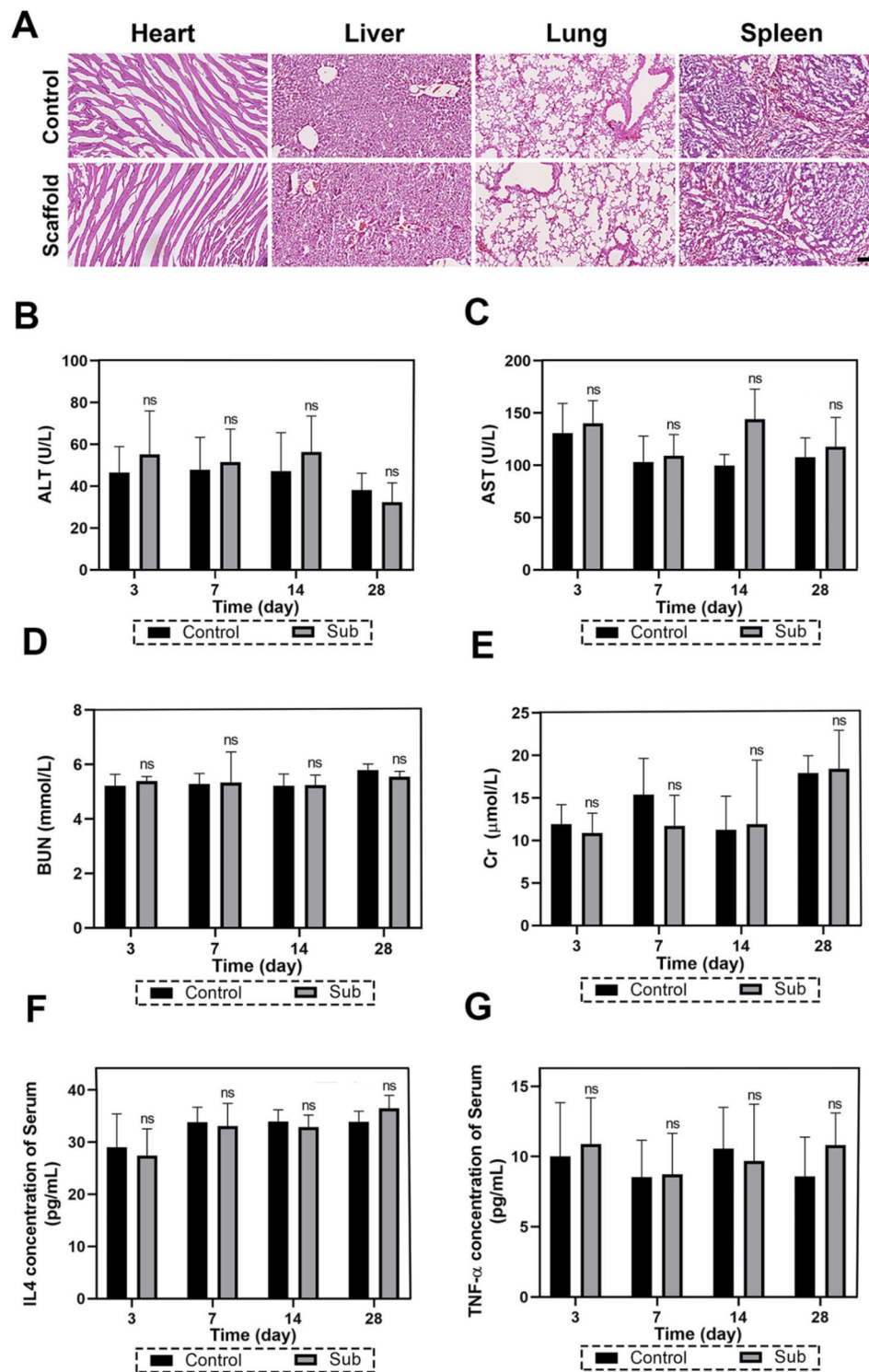


**Fig. 6** Evaluation of graft safety in mice using in vivo biosafety assays. **(A)** HE staining of mice heart, liver, spleen and kidney organ slices after 28 days of PNIPAM-GO porous scaffold transplantation. (Scale bar, 200  $\mu$ m). Evaluation of liver function as **(B)** ALT and **(C)** AST. Evaluation of kidney function as **(D)** BUN and **(E)** Cr. Levels of inflammation in the serum classified as **(F)** IL-4 and **(G)** TNF- $\alpha$ . Mean  $\pm$  SD ( $n \geq 3$ ) (ns: non-significant)

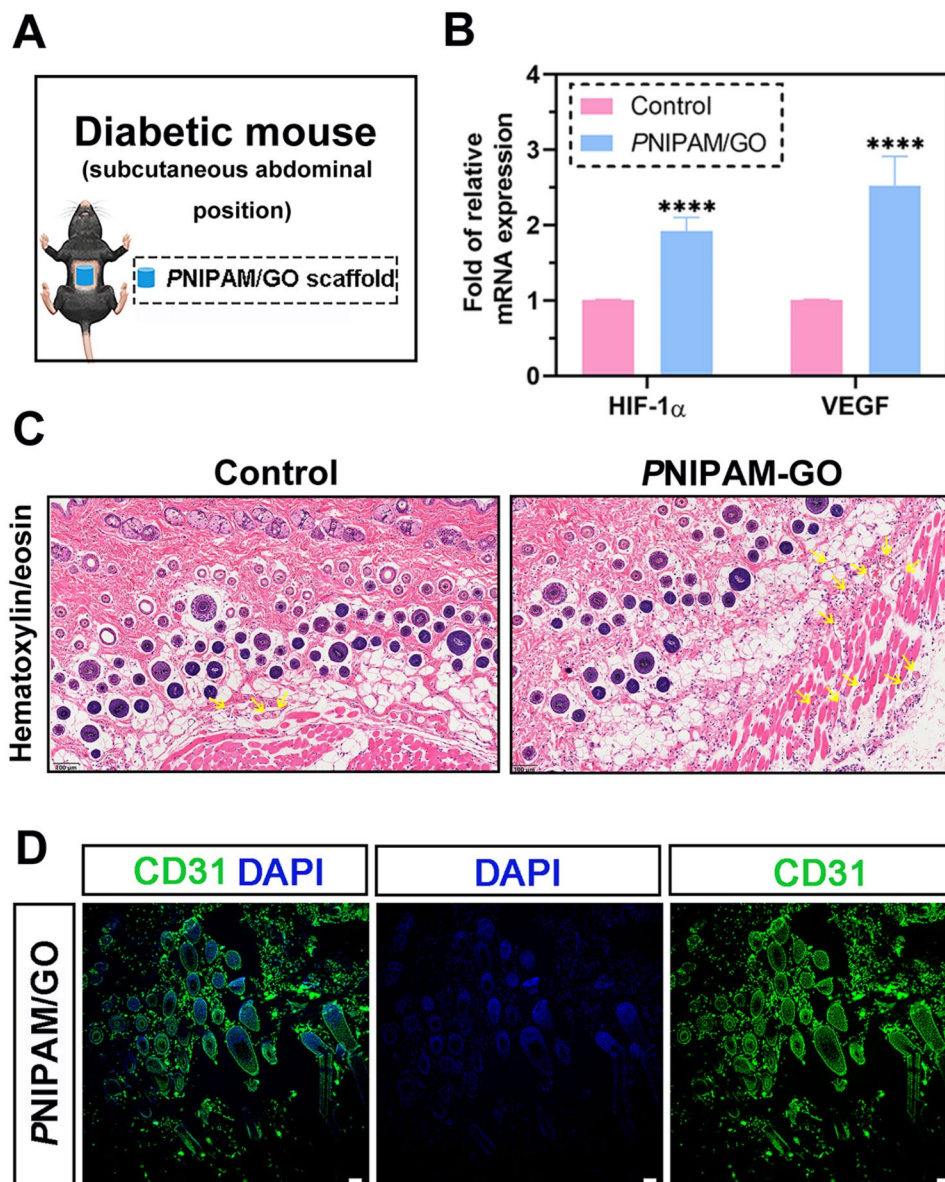


**Fig. 7** Subcutaneous blood vessel formation in mice following PNIPAM/GO scaffold implantation. **(A)** Schematic diagram of transplantation of PNIPAM/GO scaffolds in subcutaneous locations in the abdomen of diabetic mice. **(B)** The mRNA expression of subcutaneous hypoxia-inducible factor HIF-1 $\alpha$  and pro-angiogenic factor VEGF in mice after PNIPAM/GO scaffold implantation. **(C)** HE staining results of the graft and its surrounding abdominal subcutaneous tissue. The yellow arrowheads point to blood vessels with erythrocytes inside. **(D)** Confirmation of angiogenesis at abdominal subcutaneous graft sites in mice by CD31 immunofluorescence. Mean  $\pm$  SD ( $n \geq 4$ ), (\*\*\*\*:  $p < 0.0001$ ). Scale bar, 50  $\mu$ m

transplantation (Fig. S9). Furthermore, tissues and organs exhibited normalcy post-implantation of cell spheroids without rejection (Fig. S10). In vitro GSIS tests confirmed that thermally sensitive porous scaffold-encapsulated  $\beta$ -TC-6 cell spheroids exhibited robust insulin secretion, which could be modulated by NIR light to control scaffold contraction and regulate secretion. We further investigated the therapeutic efficacy of a PNIPAM-GO porous scaffold containing  $\beta$ -TC-6 cell spheroids in type I diabetic mice. Multiple, low-dose STZ injections [69] were used to create a mouse model of type 1 diabetes. After

successful modeling, islet cell spheroids were subcutaneously injected into the abdomens of diabetic mice, and insulin pharmacokinetics were monitored for 12 h. Additionally, insulin therapy effects were observed over 28 days, with concurrent recording of mice's body weights (Fig. 8A). The shrinkage group exhibited a significant decrease in blood glucose levels at 2 h compared to the diabetes model group. By 12 h post-scaffold implantation, glucose levels had returned to normal, as depicted in Fig. 8B. At 12 h, blood glucose remained significantly lower but had not yet normalized. The non-shrinkage

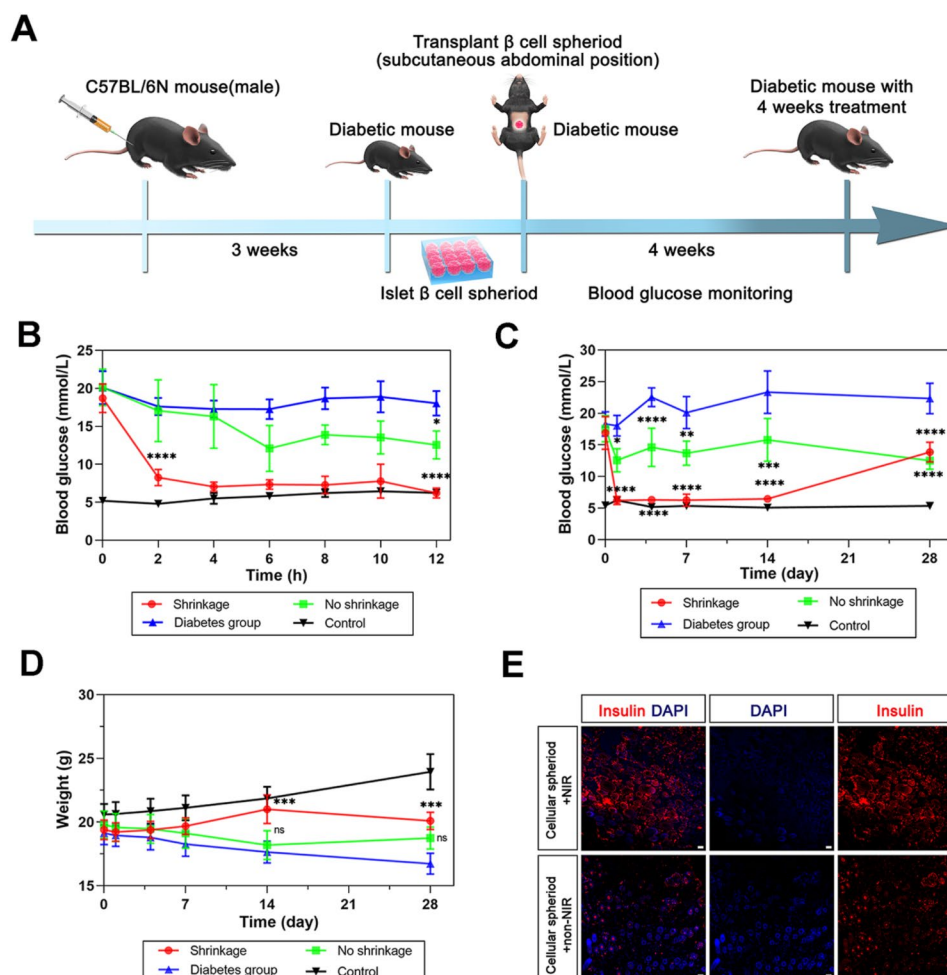


**Fig. 8** In vivo study of cell grafts for regulating blood glucose in mice. **(A)** Schematic diagram of in vivo experiments with cell grafts for glycemic control. **(B)** 12 h glucose dynamics of scaffold contraction under NIR control. **(C)** Mice with in vivo cell spheroid transplants show fluctuating blood glucose levels over a 4-week period. **(D)** Changes in mice body weight 4 weeks following in vivo cell spheroid transplanting. **(E)** Immunofluorescence map of insulin secretion in subcutaneous tissue sites of grafts after 4 weeks. Mean  $\pm$  SD ( $n \geq 4$ ), (ns: non-significant, \*:  $p < 0.05$ , \*\*:  $p < 0.01$ , \*\*\*:  $p < 0.001$ , \*\*\*\*:  $p < 0.0001$ ). Scale bar, 50  $\mu$ m

group's response to therapy did not differ significantly from that of the diabetes model group. Over 28 days, NIR irradiation at the scaffold graft site monitored the therapeutic effects of the shrinkage and non-shrinkage groups compared to the diabetic group 12 h post-implantation. Figure 8C shows that blood glucose levels in the shrinkage group returned to normal between days 1 and 14 but rose again by day 28, with a less significant decrease compared to the diabetes model group. In contrast, the non-shrinkage group showed a significant decrease in blood glucose levels from day 1 to day 28 compared to the diabetic model group, without returning to normal levels. Additionally, we investigated the therapeutic potential of PNIPAM/GO microencapsulated primary islet cells implanted subcutaneously in the abdomens of diabetic mice. We observed that NIR light had a significant therapeutic effect in controlling insulin release, thereby maintaining normal blood glucose levels in vivo for at least up

to the 28th day (Fig. S11A). To evaluate metabolic blood glucose control, we conducted an IPGTT on day 28. The results demonstrated that NIR irradiation effectively controlled the 2-hour blood glucose levels to normal during the accelerated insulin release process in diabetic mice (Fig. S11B). Figure 8D illustrates the body weight changes in mice over 28 days, showing a significant increase in the shrinkage group from day 14 to 28 compared to the diabetic model group. During days 14 to 28, the non-shrinkage group exhibited a non-significant increase in body weight compared to the diabetes model group. Figure 8E demonstrates that subcutaneous vascular insulin content at the transplantation site was significantly higher in the  $\beta$ -TC-6 cell spheroid group with NIR irradiation compared to the group without NIR irradiation. These findings indicate that  $\beta$ -TC-6 cell spheroids formed by PNIPAM-GO thermo-responsive porous scaffolds can be transplanted into mice under NIR irradiation to regulate

scaffold contraction and facilitate insulin release. Moreover, our bioinformatics research revealed that enhancing thermogenesis could serve as a potential therapeutic approach for DM. We selected 12 diabetic patients and 12 normal controls from the GEO database GSE29221 dataset and analyzed a total of 5634 differentially expressed genes (Fig. S12A). These genes were intersected with 235 thermogenesis-related genes from the Genecard database, identifying a total of 76 genes associated with thermo-regulation, including the temperature-sensitive channel protein TRPV2 (Fig. S12B and S12C). Functional annotation of differentially expressed genes using the GO database showed that genes down-regulated in DM are primarily associated with the biological process of adaptive thermogenesis (Fig. S12C). Furthermore, reduced thermogenesis in DM was supported by KEGG pathway analysis (Fig. S12D). Additionally, we observed a significantly higher expression of TRPV2 in the cell spheroid group promoted by NIR irradiation compared to the control group on days 1, 4, 7, and 14, indicating an effective photothermal induction effect (Fig. S13). In summary, when combined with the contraction of  $\beta$ -TC-6 cell spheroids induced by NIR light (as shown in Fig. 5A), this suggests a therapeutic effect on diabetic mice. Further investigation is needed to determine whether the temperature increase induced in mice by NIR light transmitting thermal energy to the thermal scaffold contributes to improved diabetic treatment.

## Conclusion

A PNIPAM-GO thermally sensitive porous scaffold is produced by depositing a dense layer of oil-in-water microspheres and subsequently curing to eliminate the oil phase, facilitated by microfluidic technology. The integration of GO and PNIPAM, with their photothermal and thermo-sensitive properties, resulted in a scaffold capable of controlled thermal contraction deformation. The controlled contraction of the scaffold facilitates the formation of cell spheroids and regulates the release of accumulated insulin. In vivo studies showed that thermally sensitive porous scaffolds effectively maintained blood glucose control over an extended period in diabetic C57BL/6 N mice. This innovative method of regulating insulin secretion from islet cells shows promise as a new approach for treating diabetes. Limitations of this study include that while we successfully prepared  $\beta$ -TC-6 cell spheroids and implanted them in mice to control insulin release effectively via photothermal mechanisms, the study is restricted to small animal models of diabetes treatment. In addition, we used the beta cell line for the main experimental investigations in this study, rather than primary cultured islets. In the future, we plan to explore the therapeutic role of primary cultured islets for use in large animal models of DM. Large animals (e.g.,

primates) possess physiological and metabolic characteristics closer to those of humans, enhancing their accuracy in modeling DM pathophysiology in humans. Our findings indicate defective expression of thermo-regulatory genes in diabetic patients and demonstrate that photothermal control stimulates the expression of TRPV2, a temperature-sensitive channel protein in  $\beta$ -TC-6 cell spheroids. However, it remains unclear whether the mechanism of photothermal regulation and the potential use of thermotherapy as a therapeutic approach for diabetes require further exploration and clarification.

## Supplementary Information

The online version contains supplementary material available at <https://doi.org/10.1186/s12951-024-02891-w>.

### Supplementary Material 1

Movie. S1 Thermally responsive shrinkage process of NIPAM-GO-PEGDA porous scaffold under NIR irradiation.

Movie. S2 Mice behavior following material transplanting.

## Acknowledgements

The authors acknowledged the financial support from "Pioneer" and "Leading Goose" R&D Program of Zhejiang (2023C04043), Joint Research Centre on Medicine of Xiangshan Hospital of Wenzhou Medical University (XSZD2024005), Wenzhou Institute, University of Chinese Academy of Sciences (WIUCASSZZXF20005, WIUCASQD2019002), the National Key Research and Development Program of China (2022YFA1207600), and National Natural Science Foundation of China (22377021, 22175182).

## Author contributions

H.Q. Li, H.B. Li and X.T. Yao designed the experiments; X.T. Yao performed synthesis and characterization of the scaffolds. X.T. Yao and Z.H. Gong created in vivo animal models. Z.H. Gong helped to draw the figures. X.T. Yao, W.Y. Yin and H.Q. Li wrote the manuscript. H.Q. Li, H.B. Li, X.T. Yao, Z.H. Gong, W.Y. Yin, L.J. Huang and D. Douroumis analyzed the data. H.Q. Li and L.J. Huang provided funding for this project. H.Q. Li and H.B. Li supervised experiments. All authors edited and approved the final manuscript.

## Data availability

No datasets were generated or analysed during the current study.

## Declarations

### Ethics approval and consent to participate

The animal experiment was conducted in accordance with the protocol approved by the Ethics Committee of the Wenzhou Institute of the Chinese Academy of Sciences (WIUCAS 20033115, 20200331).

### Consent for publication

All authors have approved the manuscript and agree to the submission.

### Competing interests

The authors declare no competing interests.

### Author details

<sup>1</sup>Joint Research Centre on Medicine, The Affiliated Xiangshan Hospital of Wenzhou Medical University, Ningbo, Zhejiang 315700, P. R. China

<sup>2</sup>Zhejiang Engineering Research Center for Tissue Repair Materials, Joint Centre of Translational Medicine, Wenzhou Institute, University of Chinese Academy of Science, Wenzhou, Zhejiang 325000, P. R. China

<sup>3</sup>School of Biomedical Engineering, Wenzhou Medical University, Wenzhou, Zhejiang 325035, P. R. China

<sup>4</sup>CAS Key Laboratory for Biomedical Effects of Nanomaterials and Nanosafety & CAS Center for Excellent in Nanoscience, Institute of High Energy Physics, Chinese Academy of Sciences, Beijing 100049, P. R. China

<sup>5</sup>Department of Pharmaceutical Sciences, Institute of Pharmacology, Zhejiang University of Technology, Hangzhou, Zhejiang 310014, P. R. China

<sup>6</sup>Centre for Research Innovation, CRI, University of Greenwich, Kent ME4 4TB, UK

<sup>7</sup>Department of Laboratory Medicine, Longhua Hospital, Shanghai University of Traditional Chinese Medicine, Shanghai 200032, P. R. China

Received: 25 March 2024 / Accepted: 1 October 2024

Published online: 26 October 2024

## References

- Cobo-Vuilleumier N, Lorenzo PI, Rodríguez NG, Herrera Gómez IG, Fuente-Martin E, López-Noriega L, Mellado-Gil JM, Romero-Zerbo SY, Baquiel M, Lachaud CC, et al. LRH-1 agonism favours an immune-islet dialogue which protects against diabetes mellitus. *Nat Commun*. 2018;9(1):1488.
- Tauschmann M, Hovorka R. Technology in the management of type 1 diabetes mellitus - current status and future prospects. *Nat Reviews Endocrinol*. 2018;14(8):464–75.
- Eizirik DL, Pasquali L, Cnop M. Pancreatic  $\beta$ -cells in type 1 and type 2 diabetes mellitus: different pathways to failure. *Nat Reviews Endocrinol*. 2020;16(7):349–62.
- Lansberry TR, Stabler CL. Immunoprotection of cellular transplants for auto-immune type 1 diabetes through local drug delivery. *Adv Drug Deliv Rev*. 2024;206:115179.
- Greenhill C. Stem-cell derived pancreatic endoderm cells in the treatment of T1DM. *Nat Reviews Endocrinol*. 2022;18(2):67.
- Rocha DS, Manucci AC, Bruni-Cardoso A, Kowaltowski AJ, Vilas-Boas EA. A practical and robust method to evaluate metabolic fluxes in primary pancreatic islets. *Mol Metabol*. 2024;83:101922.
- Bloch K, Bloch O, Tarasenko I, Lazard D, Rapoport M, Vardi P. A strategy for the engineering of insulin producing cells with a broad spectrum of defense properties. *Biomaterials*. 2011;32(7):1816–25.
- Hall KK, Gattás-Asfura KM, Stabler CL. Microencapsulation of islets within alginate/poly(ethylene glycol) gels cross-linked via Staudinger ligation. *Acta Biomater*. 2011;7(2):614–24.
- K SC SAF. Engineering Vascularized Islet Macroencapsulation devices: an in vitro platform to Study Oxygen Transport in Perfused immobilized pancreatic Beta cell cultures. *Front Bioeng Biotechnol*. 2022;10:884071.
- Sykes M, Sachs DH. Progress in xenotransplantation: overcoming immune barriers. *Nat Rev Nephrol*. 2022;18(12):745–61.
- Asthana A, Chaimov D, Tamburrini R, Gazia C, Gallego A, Lozano T, Heo JH, Byers LN, Tomei A, Fraker CA, et al. Decellularized human pancreatic extracellular matrix-based physiologic microenvironment for human islet culture. *Acta Biomater*. 2023;171:261–72.
- Krishtul S, Skitel Moshe M, Kovrigina I, Baruch L, Machluf M. ECM-based bioactive microencapsulation significantly improves islet function and graft performance. *Acta Biomater*. 2023;171:249–60.
- Derakhshankhah H, Sajadimajid S, Jahanshahi F, Samsonchi Z, Karimi H, Hajizadeh-Saffar E, Jafari S, Razmi M, Malvajerd SS, Bahrami G, et al. Immunoen지니어링 Biomaterials in Cell-based therapy for type 1 diabetes. *Tissue Eng Part B Reviews*. 2022;28(5):1053–66.
- Weaver JD, Headen DM, Coronel MM, Hunckler MD, Shirwan H, García AJ. Synthetic poly(ethylene glycol)-based microfluidic islet encapsulation reduces graft volume for delivery to highly vascularized and retrievable transplant site. *Am J Transplant*. 2019;19(5):1315–27.
- Grapin-Botton A. Three-dimensional pancreas organogenesis models. *Diabetes Obes Metab*. 2016;18(Suppl 1):33–40.
- Gebe JA, Preisinger A, Gooden MD, D'Amico LA, Vernon RB. Local, controlled release in vivo of vascular endothelial growth factor within a Subcutaneous Scaffolded Islet Implant reduces early islet necrosis and improves performance of the graft. *Cell Transplant*. 2018;27(3):531–41.
- Stamateris RE, Sharma RB, Kong Y, Ebrahimipour P, Panday D, Ranganath P, Zou B, Levitt H, Parambil NA, O'Donnell CP, et al. Glucose induces mouse  $\beta$ -Cell proliferation via IRS2, MTOR, and cyclin D2 but not the insulin receptor. *Diabetes*. 2016;65(4):981–95.
- Kim J, Shim IK, Hwang DG, Lee YN, Kim M, Kim H, Kim SW, Lee S, Kim SC, Cho DW, et al. 3D cell printing of islet-laden pancreatic tissue-derived extracellular matrix bioink constructs for enhancing pancreatic functions. *J Mater Chem B*. 2019;7(10):1773–81.
- Jiang K, Chaimov D, Patel SN, Liang JP, Wiggins SC, Samojlik MM, Rubiano A, Simmons CS, Stabler CL. 3-D physiologic microenvironment for rodent and human islet culture. *Biomaterials*. 2019;198:37–48.
- Duin S, Schütz K, Ahlfeld T, Lehmann S, Lode A, Ludwig B, Gelinsky M. 3D bioprinting of functional islets of Langerhans in an Alginate/Methylcellulose Hydrogel Blend. *Adv Healthc Mater*. 2019;8(7):e1801631.
- Farina M, Chua CYX, Ballerini A, Thekkedath U, Alexander JF, Rhudy JR, Torchio G, Fraga D, Pathak RR, Villanueva M, et al. Transcutaneously refillable, 3D-printed biopolymeric encapsulation system for the transplantation of endocrine cells. *Biomaterials*. 2018;177:125–38.
- Weaver JD, Headen DM, Hunckler MD, Coronel MM, Stabler CL, García AJ. Design of a vascularized synthetic poly(ethylene glycol) macroencapsulation device for islet transplantation. *Biomaterials*. 2018;172:54–65.
- Li Q, Jiao Y. Ultrafast Photothermal Actuators with a large helical curvature based on ultrathin GO and biaxially oriented PE films. *ACS Appl Mater Interfaces*. 2022;14(50):55828–38.
- Martinez-Moro M, Jencyk J, Jurga S, Moya SE. Kinetics of the thermal response of poly(N-isopropylacrylamide co methacrylic acid) hydrogel microparticles under different environmental stimuli: a time-lapse NMR study. *J Colloid Interface Sci*. 2020;580:439–48.
- Montalbano G, Toumpaniari S, Popov A, Duan P, Chen J, Dalgarno K, Scott WE, Ferreira AM. Synthesis of bioinspired collagen/alginate/fibrin based hydrogels for soft tissue engineering. *Materials science & engineering C, Materials for biological applications* 2018, 91:236–246.
- Capitano ML, Ertel BR, Repasky EA, Ostberg JR. Winner of the 2007 society for Thermal Medicine Young Investigator Award. Fever-range whole body hyperthermia prevents the onset of type 1 diabetes in non-obese diabetic mice. *Int J Hyperthermia*. 2008;24(2):141–9.
- Lee P, Smith S, Linderman J, Courville AB, Brychta RJ, Dieckmann W, Werner CD, Chen KY, Celi FS. Temperature-acclimated brown adipose tissue modulates insulin sensitivity in humans. *Diabetes*. 2014;63(11):3686–98.
- Xia Z, Sato A, Hughes MA, Cherry GW. Stimulation of fibroblast growth in vitro by intermittent radiant warming. *Wound Repair Regen*. 2000;8(2):138–144.
- Hughes MA, Tang C, Cherry GW. Effect of intermittent radiant warming on proliferation of human dermal endothelial cells in vitro. *J Wound Care*. 2003;12(4):135–7.
- Huang R, Li S, Tian C, Zhou P, Zhao H, Xie W, Xiao J, Wang L, Habimana JD, Lin Z, et al. Thermal stress involved in TRPV2 promotes tumorigenesis through the pathways of HSP70/27 and PI3K/Akt/mTOR in esophageal squamous cell carcinoma. *Br J Cancer*. 2022;127(8):1424–39.
- Shao C, Liu Y, Chi J, Wang J, Zhao Z, Zhao Y. Responsive Inverse Opal Scaffolds with Biomimetic Enrichment Capability for Cell Culture. *Research* (Washington, DC) 2019, 2019:9783793.
- Wang LH, Marfil-Garza BA, Ernst AU, Pawlick RL, Pepper AR, Okada K, Epel B, Viswakarma N, Kotecha M, Flanders JA, et al. Inflammation-induced subcutaneous neovascularization for the long-term survival of encapsulated islets without immunosuppression. *Nat Biomedical Eng*. 2023. <https://doi.org/10.1038/s41551-023-01145-8>.
- Song W, Chiu A, Wang LH, Schwartz RE, Li B, Bouklas N, Bowers DT, An D, Cheong SH, Flanders JA, et al. Engineering transferrable microvascular meshes for subcutaneous islet transplantation. *Nat Commun*. 2019;10(1):4602.
- Liang LT, Song W, Zhang C, Li Z, Yao B, Zhang MD, Yuan XY, Jirigala E, Fu XB, Huang S, et al. [Effects of in situ cross-linked graphene oxide-containing gelatin methacrylate anhydride hydrogel on wound vascularization of full-thickness skin defect in mice]. *Zhonghua shao shang za zhi = Zhonghua Shaoshang zazhi = Chinese J Burns*. 2022;38(7):616–28.
- Ding X, Yu Y, Yang C, Wu D, Zhao Y. Multifunctional GO Hybrid Hydrogel Scaffolds for Wound Healing. *Research* (Washington, DC) 2022, 2022:9850743.
- McMasters J, Poh S, Lin JB, Panitch A. Delivery of anti-inflammatory peptides from hollow PEGylated poly(NIPAM) nanoparticles reduces inflammation in an ex vivo osteoarthritis model. *J Control Release*. 2017;258:161–70.
- Ghandforoushan P, Hanaee J, Aghazadeh Z, Samiei M, Navali AM, Khatibi A, Davaran S. Novel nanocomposite scaffold based on gelatin/PLGA-PEG-PLGA hydrogels embedded with TGF- $\beta$ 1 for chondrogenic differentiation of human dental pulp stem cells in vitro. *Int J Biol Macromol*. 2022;201:270–87.

38. Chao L, Jiao C, Liang H, Xie D, Shen L, Liu Z. Analysis of Mechanical properties and Permeability of Trabecular-Like Porous Scaffold by Additive Manufacturing. *Front Bioeng Biotechnol*. 2021;9:779854.
39. Kelly CN, Wang T, Crowley J, Willis D, Pelletier MH, Westrick ER, Adams SB, Gall K, Walsh WR. High-strength, porous additively manufactured implants with optimized mechanical osseointegration. *Biomaterials*. 2021;279:121206.
40. Tuan HNA, Nhu VTT. Synthesis and Properties of pH-Thermo Dual Responsive Semi-IPN Hydrogels based on N,N'-Diethylacrylamide and Itaconic Acid. *Polymers*. 2020;12(5):1139.
41. Narayanan A, Menefee JR, Liu Q, Dhinojwala A, Joy A. Lower critical solution temperature-driven self-coacervation of Nonionic Polyester underwater adhesives. *ACS Nano*. 2020;14(7):8359–67.
42. Tudor A, Florea L, Gallagher S, Burns J, Diamond D. Poly(ionic Liquid) Semi-interpenetrating Network Multi-responsive Hydrogels. *Sensors*. 2016;16(2):219.
43. Li H, Liu B, Lian L, Zhou J, Xiang S, Zhai Y, Chen Y, Ma X, Wu W, Hou L. High dose expression of heme oxygenase-1 induces retinal degeneration through ER stress-related DDIT3. *Mol Neurodegeneration*. 2021;16(1):16.
44. Hwang DG, Jo Y, Kim M, Yong U, Cho S, Choi YM, Kim J, Jang J. A 3D bioprinted hybrid encapsulation system for delivery of human pluripotent stem cell-derived pancreatic islet-like aggregates. *Biofabrication*. 2021;14(1):014101.
45. Changson K, Pang Y, Matsumoto H, Hong H, Wüthrich P, Sun W, Sakai Y. 3D perfusion culture of mouse insulinoma in macro-porous scaffolds enhanced insulin production response. *Int J Artif Organs*. 2022;45(1):96–102.
46. Skrzypek K, Groot Nibbelink M, van Lente J, Buitinga M, Engelse MA, de Koning EJP, Karperien M, van Apeldoorn A, Stamatialis D. Pancreatic islet macroencapsulation using microwell porous membranes. *Sci Rep*. 2017;7(1):9186.
47. Long Y, Yan L, Dai H, Yang D, Wu X, Dong X, Liu K, Wei W, Chen Y. Enhanced proliferation and differentiation of neural stem cells by peptide-containing temperature-sensitive hydrogel scaffold. *Mater Sci Eng C Mater Biol Appl*. 2020;116:111258.
48. Carreño G, Pereira A, Ávila-Salas F, Marican A, Andrade F, Roca-Melendres MM, Valdés O, Vijayakumar S, Schwartz S, Abasolo I, et al. Development of on-demand thermo-responsive hydrogels for anti-cancer drugs sustained release: rational design, in silico prediction and in vitro validation in colon cancer models. *Mater Sci Eng C Mater Biol Appl*. 2021;131:112483.
49. Kumar GG, Hashmi S, Karthikeyan C, GhavamiNejad A, Vatankhah-Varnoosfaderani M, Stadler FJ. Graphene oxide/carbon nanotube composite hydrogels-versatile materials for microbial fuel cell applications. *Macromol Rapid Commun*. 2014;35(21):1861–5.
50. Liang JP, Accolla RP, Soundirarajan M, Emerson A, Coronel MM, Stabler CL. Engineering a macroporous oxygen-generating scaffold for enhancing islet cell transplantation within an extrahepatic site. *Acta Biomater*. 2021;130:268–80.
51. Kang W, Liang J, Liu T, Long H, Huang L, Shi Q, Zhang J, Deng S, Tan S. Preparation of silane-dispersed graphene crosslinked vinyl carboxymethyl chitosan temperature-responsive hydrogel with antibacterial properties. *Int J Biol Macromol*. 2022;200:99–109.
52. Mondal S, Kumari A, Mitra K, Verma A, Saha S, Maiti B, Singh R, Manna PP, Maiti P, Watanabe H, et al. Biocompatible thermoresponsive N-isopropyl-N-(3-(isopropylamino)-3-oxopropyl)acrylamide-based random copolymer: synthesis and studies of its composition dependent properties and anticancer drug delivery efficiency. *J Mater Chem B*. 2022;10(41):8462–77.
53. Tsuchiya M, Kurashina Y, Onoe H. Eye-recognizable and repeatable biochemical flexible sensors using low angle-dependent photonic colloidal crystal hydrogel microbeads. *Sci Rep*. 2019;9(1):17059.
54. Gonzalez-Obeso C, Rodriguez-Cabello JC, Kaplan DL. Fast and reversible crosslinking of a silk elastin-like polymer. *Acta Biomater*. 2022;141:14–23.
55. Kwon M, Yang J, Kim H, Joo H, Joo SW, Lee YS, Lee HJ, Jeong SY, Han JH, Paik HJ. Controlling Graphene wrinkles through the phase transition of a polymer with a low critical solution temperature. *Macromol Rapid Commun*. 2021;42(23):e2100489.
56. Song F, Gong J, Tao Y, Cheng Y, Lu J, Wang H. A robust regenerated cellulose-based dual stimuli-responsive hydrogel as an intelligent switch for controlled drug delivery. *Int J Biol Macromol*. 2021;176:448–58.
57. Arcos-Hernandez M, Naidjonoka P, Butler SJ, Nylander T, Ståhlbrand H, Jannasch P. Thermoresponsive glycopolymers based on enzymatically synthesized Oligo- $\beta$ -Mannosyl Ethyl methacrylates and N-Isopropylacrylamide. *Biomacromolecules*. 2021;22(6):2338–51.
58. Gong X, Hou C, Zhang Q, Li Y, Wang H. Thermochromic hydrogel-functionalized textiles for synchronous visual monitoring of On-Demand In Vitro Drug Release. *ACS Appl Mater Interfaces*. 2020;12(46):51225–35.
59. Chen C, Wang Y, Zhang H, Zhang H, Dong W, Sun W, Zhao Y. Responsive and self-healing structural color supramolecular hydrogel patch for diabetic wound treatment. *Bioactive Mater*. 2022;15:194–202.
60. Velasco-Mallorquí F, Rodríguez-Comas J, Ramón-Azcón J. Cellulose-based scaffolds enhance pseudoislets formation and functionality. *Biofabrication*. 2021;13(3):035044.
61. Liu C, Guo X, Ruan C, Hu H, Jiang BP, Liang H, Shen XC. An injectable thermosensitive photothermal-network hydrogel for near-infrared-triggered drug delivery and synergistic photothermal-chemotherapy. *Acta Biomater*. 2019;96:281–94.
62. Sun P, Huang T, Wang X, Wang G, Liu Z, Chen G, Fan Q. Dynamic-covalent hydrogel with NIR-Triggered Drug Delivery for Localized Chemo-Photothermal Combination Therapy. *Biomacromolecules*. 2020;21(2):556–65.
63. Kim M, Kim H, Lee YS, Lee S, Kim SE, Lee UJ, Jung S, Park CG, Hong J, Doh J, et al. Novel enzymatic cross-linking-based hydrogel nanofilm caging system on pancreatic  $\beta$  cell spheroid for long-term blood glucose regulation. *Sci Adv*. 2021;7(26):eabf7832.
64. Zhang Y, Yang J, Zhang J, Li S, Zheng L, Zhang Y, Meng H, Zhang X, Wu Z. A bio-inspired injectable hydrogel as a cell platform for real-time glycaemic regulation. *J Mater Chem B*. 2020;8(21):4627–41.
65. Liu J, Liu B, Min S, Yin B, Peng B, Yu Z, Wang C, Ma X, Wen P, Tian Y, et al. Biodegradable magnesium alloy WE43 porous scaffolds fabricated by laser powder bed fusion for orthopedic applications: process optimization, in vitro and in vivo investigation. *Bioactive Mater*. 2022;16:301–19.
66. Li X, Liu J, Zhao Y, Xu N, Lv E, Ci C, Li X. 1,25-dihydroxyvitamin D3 ameliorates lupus nephritis through inhibiting the NF- $\kappa$ B and MAPK signalling pathways in MRL/lpr mice. *BMC Nephrol*. 2022;23(1):243.
67. Yang L, Zhao M, Chen W, Zhu J, Xu W, Li Q, Pu K, Miao Q. A highly bright Near-Infrared Afterglow Luminophore for Activatable Ultrasensitive in vivo imaging. *Angewandte Chemie (International ed English)*. 2024;63(4). e202313117.
68. Pan C, Xu R, Chen J, Zhang Q, Deng L, Hong Q. A CO-releasing coating based on carboxymethyl chitosan-functionalized graphene oxide for improving the anticorrosion and biocompatibility of magnesium alloy stent materials. *Int J Biol Macromol*. 2024;271(Pt 2):132487.
69. Sarnobat D, Moffett RC, Ma J, Flatt PR, McClenaghan NH, Tarasov AI. Taurine rescues pancreatic  $\beta$ -cell stress by stimulating  $\alpha$ -cell transdifferentiation. *Biofactors*. 2023;49(3):646–62.

## Publisher's note

Springer Nature remains neutral with regard to jurisdictional claims in published maps and institutional affiliations.